

**SYNTHESIS AND MECHANICAL CHARACTERIZATION OF
TRANSVERSELY ISOTROPIC NANOPOROUS PLATINUM**

A Thesis
Presented to
The Academic Faculty

by

Yuan Li

In Partial Fulfillment
of the Requirements for the Degree
Master of Science in the
George W. Woodruff School of Mechanical Engineering

Georgia Institute of Technology
December 2011

**SYNTHESIS AND MECHANICAL CHARACTERIZATION OF
TRANSVERSELY ISOTROPIC NANOPOROUS PLATINUM**

Approved by:

Dr. Antonia Antoniou, Advisor
School of Mechanical Engineering
Georgia Institute of Technology

Dr. Olivier Pierron
School of Mechanical Engineering
Georgia Institute of Technology

Dr. Ting Zhu
School of Mechanical Engineering
Georgia Institute of Technology

Date Approved: November 9, 2011

To My Beloved Parents and Grandparents

ACKNOWLEDGEMENTS

I would like to start off by expressing my thanks to my advisor, Dr. Antoniou, who guided me through obstacles, encouraged me when hardiness appears, and shared the joy of achievements all the way to this finishing point of M.S. degree. The systematic training of scientific research she provided to me has benefit and will continue to benefit my entire life. I'm looking forward for the further guidance and support from her in my Ph.D. study.

Secondly, I am very grateful to members of my thesis reading committee, Dr. Ting Zhu and Dr. Olivier Pierron for their gracious participation. I've taken courses from both of the professors and the knowledge I learnt in class also greatly facilitate my research.

Next, I would like to thank my fellow group member and my friend Ran Liu, for the valuable discussion and partnership both in class and research projects in the past two years. Also, I would love to thank Mr. Walter Henderson and Mr. Eric Woods and other members in Nanotechnology Research Center (Georgia Tech) for the equipment training and help.

Finally, deepest thanks to my entire family especially my parents and my grandparents. Their love and care provided me enormous motivation in the pursuit of my dreams.

TABLE OF CONTENTS

ACKNOWLEDGEMENTS	IV
LIST OF TABLES	VII
LIST OF FIGURES.....	VIII
SUMMARY	XI
CHAPTER 1 INTRODUCTION	1
1.1 Nanoporous Metals	1
1.2 Motivation and Performed Work.....	1
1.3 Background	2
1.3.1 Synthesis.....	2
1.3.1.2 Dealloying.....	5
1.3.1.2.1 Critical Potential.....	5
1.3.1.2.2 Dealloying Mechanism.....	6
1.3.2 Mechanical Properties of NP Metal Foams.....	9
1.4 Thesis Organization	13
CHAPTER 2 SYNTHESIS OF TRANSVERSELY ISOTROPIC NANOPOROUS PLATINUM.....	15
2.1 Introduction	15
2.2 Experimental Methodology.....	16
2.3 Results and Discussion	19
2.4 Summary	30
CHAPTER 3 EXAMINATION OF DEALLOYING INITIATION IN AN AMORPHOUS Pt_xSi_{1-x} ALLOY	31
3.1 Introduction	31
3.3 Results and discussion	33
3.4 Summary	38

CHAPTER 4 MECHANICAL BEHAVIOR OF TRANSVERSELY ISOTROPIC NP PLATINUM FOAM.....	39
4.1 Introduction	39
4.2.1. Sample preparation	40
4.2.2. Microstructural characterization and mechanical testing.....	40
4.3 Results and discussion	41
4.4 Summary	55
CHAPTER 5 SUMMARY AND FUTURE WORK.....	56
REFERENCES.....	58

LIST OF TABLES

Table 1.1 Literature review of precursor alloy and dealloying electrolyte	4
Table 2.1 A summary of sample parameters before dealloying	16
Table 4.1 The relative densities of various cell struts	51

LIST OF FIGURES

Figure 1.1 Three types of NP Pt synthesized by controlling experimental parameters	3
Figure 1.2 One example curve of current density as a function of applied voltage during dealloying	6
Figure 1.3 Schematic representation on an atomic scale of the surface of an alloy composed of dissolvable A atoms and noble B atoms. K is a kink site on surface step; N is a non-kink site on a step; T is a terrace site.[32]	7
Figure 2.1 SEM (a) plan and (b) 52° tilt views of Voronoi type nanoporous platinum foam with 0.7V dealloying voltage and 200s dealloying period, (c) plan view image of the radial-like strut of Voronoi-type NP Pt foam.....	17
Figure 2.2 (a) Current density as a function of applied voltage during dealloying of Pt _{0.33} Si _{0.67} (Sample Set A). E ₀ is the critical potential. (b) Current density as a function of time during dealloying of Pt _{0.33} Si _{0.67} with different dealloying voltages and the resulting plan view SEM image for: (c) 0.3V; (d) 0.6V; (e) 0.7V; (f) 0.9V.....	21
Figure 2.3 Normalized Voronoi polyhedral diameter as a function of normalized dealloying potential for both sample sets, where D _p is the well-established polyhedral diameter and D ₀ =10 nm. The dashed line is a simple data fit. The shaded regions mark where no Voronoi polyhedra can form.	23
Figure 2.4 (a) Plan view SEM of the same region monitored at (a) t=0s, (b) t=60s, (c) t=120s during dealloying at E = 0.5 V. (d) Mathematical prediction (t >150s) of the polyhedra boundaries using the initiation sites as input. Prediction is superimposed on the plan view SEM image obtained at t = 120s (e) 52° tilt cross-section view near a dealloying site. White arrow marks the location where NP Pt foam has formed.	26
Figure 2.5 (a) Schematic 3-D and cross section views for the dealloying front progression at different time intervals. (b) Experimental measurements of dealloying front radius as a function of time for two different samples in Sample Set A. The red dash lines represent the phenomenological model predictions for the largest (670nm) and smallest (100nm) possible polygon dimensions.	27
Figure 3.1 Amorphous state SEM (a) and AFM scan (c) and same region As-dealloyed (dealloying voltage 0.5V, 120s) SEM (b) and AFM scan (d). Surface roughness analysis of O-O cut (e), showing at a fixed voltage, dealloying initiate preferentially at high roughness spots.	34

Figure 3.2 Images of a sample from sample set A dealloyed at 0.5V for 120s. Amorphous state (0s) SEM plan view (a) and its enlarged boxed area (b), corresponding location AFM scan image (e) and same enlarged boxed area (f). As-dealloyed (120s) state SEM plan view (c) and its enlarged boxed area (d), AFM scan image (g) and same enlarged boxed area (h) 35

Figure 3.3 Images of a sample from sample set A dealloyed at 0.7V for 120s. Amorphous (0s) state SEM plan view (a) and its enlarged boxed area (b), corresponding location AFM scan image (e) and same enlarged boxed area (f). As-dealloyed (120s) state SEM plan view (c) and its enlarged boxed area (d), AFM scan image (g) and same enlarged boxed area (h) 36

Figure 3.4 The upper images are x-x and y-y cut (referring to Figs. 3.2 and 3.3) surface roughness analysis for dealloying voltage 0.5V, the lower counterparts for 0.7V. Inserted images are the corresponding initial roughness. 37

Figure 4.1 Schematic drawing of a typical cross-section of transverse isotropic NP Pt foam synthesized in this work..... 42

Figure 4.2 SEM cross-sectional images with (a) big Voronoi polyhedron size where radial emanation of ligaments and pores well preserved and its enlarged view (b); (f) small Voronoi polyhedron size where ligaments and pores align vertically through the thickness and its enlarged view (g); (c) polyhedron size in between shows a transformational morphology and its enlarged views (d) and (e). For clearer demonstration, spherical parts of dealloying fronts and several ligaments and pores are highlighted in red dotted line 43

Figure 4.3 Hardness values (including standard deviation) as a function of (a) indentation depth δ and (b) indentation depth δ normalized by ligament size l for as-dealloyed samples in sample set B (detailed in Table 2.1) and isotropic open cell sample. Polygon sizes (D_p) and ligament length (l) are indicated in the legend. 44

Figure 4.4 (a) Reduced modulus (including standard deviation) as a function of indentation depth δ . Calculated Young's modulus as a function of (b) indentation depth δ and (c) indentation depth δ normalized by ligament size l for as-dealloyed samples in sample set B (detailed in Table 2.1) and isotropic open cell sample. 46

Figure 4.5 Under a general in plane stress state, (a) rectangular (elongated) cell periodic structure and (b) a unit cell; (c) square (isotropic) cell and (d) a unit cell; (e) half circle (radially distributed ligament) cell and a representative local part (f) 47

Figure 4.6 Ligaments under compression with no consideration of lateral forces for (a) isotropic cell ligament; (b) elongated cell ligament and (c) radially distributed cell ligament 52

Figure 4.7 ABAQUS modeling of (a) isotropic cell structure, (b) elongated cell structure and (c) radial cell structure with center loading (position 1) and eccentric loading at different locations (position 2,3,4, with small, medium, and large amount of shift of loading center from the structure center point, separately). All the three structure have same relative density. 53

Figure 4.8 Stiffness comparison for different cell geometries of several loading conditions. Small, medium and large in parenthesis after eccentric loading means the amount of shift of loading center from the structure center point. Relative densities are identical for all cases. 54

SUMMARY

Nanoporous (NP) metal foams combine desirable characteristics of metals with unique nanoarchitectural features to yield weight normalized properties far superior than either dense metals or bulk metal foams. Due to their high surface to volume ratios these structures show great promise as components of fuel cells, as sensors and have been suggested for use in biological applications, for example as antimicrobial scaffolds or as platforms on which to explore biological material behavior. While most NP metal foams are isotropic, structures with anisotropic features spanning different length scales can further extend applications. This work examines the parameters controlling the synthesis of transversely isotropic NP Platinum foam by dealloying an amorphous Pt-Si alloy. The structure that is examined in this work is hierarchical with Voronoi polyhedra that form on the free surface and under each polyhedral hyper-structure, nanocrystalline NP Pt foam forms with radial struts of length ~ 60 nm and grain size of 5 nm. The size of the polyhedra can be tailored by changing the dealloying potential. In turn, the mechanical properties of these structures as assessed by nanoindentation can range from 1 to 3GPa depending on the geometric arrangement of the struts. Finally, the initiation location of these structures and the relationship between electrochemical parameters and dealloying front evolution is examined.

CHAPTER 1

INTRODUCTION

1.1 Nanoporous Metals

Nanoporous (NP) metal foams with their large surface to volume ratios show great promise as key components for energy and biological applications. For example, platinum (Pt) plated NP gold used as a catalyst in a Proton Exchange Membrane fuel cell shows a marked increase in power density when compared to conventional Pt catalyst [1]. NP Ni foam could dramatically enhance the high-rate discharge performance of rechargeable batteries given that Ni foams with mm-sized pores have been reliably used as current collectors in Ni-metal hydride batteries for the last 30 years. In addition, NP metal foams have been suggested in biological applications, for example as antimicrobial scaffolds[2] or platforms on which to explore biological material behavior[3]. Some of their very attractive applications (e.g. sensors) can be further extended by utilizing NP metal structure with anisotropic features.

The following pages describe the performed work and the motivation behind it. In addition, an overview of parameters that influence synthesis of NP metals foams, their mechanical properties as well as an overview of how the thesis will be organized will be given.

1.2 Motivation and Performed Work

Recent work on the study of transport mechanisms in transmembrane proteins [4] has revealed that while certain morphologies of NP metal foams are ideal stable templates, other morphologies disintegrate after brief exposures in an aqueous environment. The more stable structures were found to be transversely isotropic NP Pt foams. Yet, there is very little work done on the synthesis and mechanical behavior of

NP metal foams with anisotropic features. To date, most research work on NP metal foams has focused on the formation and mechanical behavior of isotropic NP Au [5-10], NP Pt [11-14] and NP Cu [15-18]. While there has been some work on the synthesis of anisotropic NP metals by selective etching of pre-existing phases of an alloy [19, 20], there is very little work done comparing differences in properties of isotropic and anisotropic structures with nanosized struts. An experimental framework is embraced here to:

- 1) Understand the conditions that control the synthesis of anisotropic NP Pt structures from a homogeneous amorphous mixture of Pt_xSi_{1-x} without any geometrical boundaries by varying either initial alloy conditions or electrochemical parameters.
- 2) Explore the origin of the formation of the transverse anisotropy and develop an understanding on how to control anisotropy.
- 3) Measure the mechanical properties of NP Pt of various isotropic and transverse isotropic morphologies using instrumented indentation.

The study can be important in understanding how the NP Pt foam dealloyed from amorphous alloys to be further modified experimentally to potentially improve their functionality and biocompatibility in a variety of applications.

1.3 Background

1.3.1 Synthesis

NP metal foams with pores and ligaments below 100 nm cannot be easily synthesized by sintering, casting or powder metallurgy. While several techniques to synthesize NP metal foams are possible (e.g. combustion synthesis [21] or nanosmelting[22]), the most commonly used synthesis approach (as first pointed out by Forty, and adapted by following researchers) is electrochemical dealloying, a controlled corrosion technique

that consistently produces struts and pores with the same range of dimensions. During dealloying, element(s) of an alloy can be selectively dissolved in an aqueous solution and under certain conditions, more noble elements self assemble to form a three dimensional network of struts and pores [8, 10, 23-26]. Taking advantage of an instability at the solid/liquid interface is an ingenious way to self assemble materials and it has been shown to produce relatively large free standing samples with nanosized features [5, 6, 27]. A two step NP foam synthesis process is involved in most of the literature: precursor alloy preparation and subsequent electrochemical dealloying. A variety of NP foam morphologies could be synthesized by controlling experimental parameters in both the two steps. For example, several types of NP Pt we are able to synthesize in lab are shown in Figure 1.1.

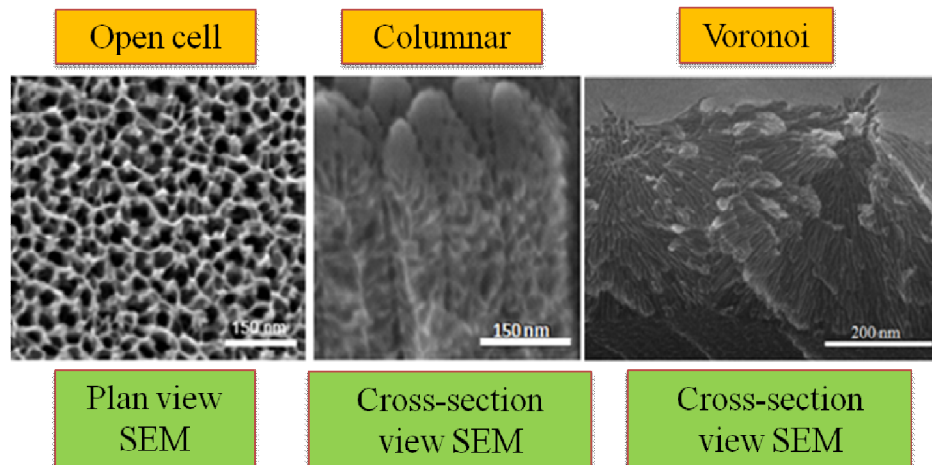


Figure 1.1 Three types of NP Pt synthesized by controlling experimental parameters

1.3.1.1 Precursor Alloy

Co-sputtering [13, 14] and coevaporation [12] are typically used for preparing thin films of an initial alloy that can be subsequently dealloyed in a corrosive environment [6]. Note that even though two phase precursor alloy such as Ni-based superalloy (with γ or γ' phases to be afterwards dealloyed to form NP Ni) has been reported in the literature [20], in most cases homogeneous single phase alloys must

always be finally achieved prior to dealloying. Inhomogeneities in the initial alloy are typically overcome by heat treatments [28]. The chosen of precursor species is also critical: one species is typically nobler than the other/others by several hundred mill volts [12] such that when applying intermediate potential (higher than the less noble species but significantly lower than the more noble species), the less noble species could be easily electrochemically etched from the precursor alloy . Under the above mentioned guidance, numerous systems have been found to be able to form NP metals. For example, the precursor alloys to synthesize NP Au, NP Cu, NP Cd, NP Pt and NP Ni are summarized in Table 1.1. It is also important to keep in mind that selective dissolution can occur for a range of composition ranges for the more noble metal [29]. Therefore, careful control of the initial alloy composition and state is necessary to produce uniform NP metal foam.

Table 1.1 Literature review of precursor alloy and dealloying electrolyte

Foam	Precursor alloy	Electrolyte	Ref.
NP Au	Au-Ag	HNO ₃ Acid	[10, 30-36]
	Au-Cu	H ₂ SO ₄ Acid	[37, 38]
NP Cu	Cu-Mn	NaCl Solutions	[15, 16]
	Cu-Zn	NaCl Solutions	[17, 18]
NP Cd	Cd-Mg	NaClO ₄ solutions	[39, 40]
NP Pt	Pt-Cu	H ₂ SO ₄ Acid	[11]
	Pt-Si	HF Acid	[12, 41]
	Pt-Si-Ni	HF Acid	[13, 14]
NP Ni	Ni-Cu	Sulfamate Solutions	[42]

1.3.1.2 Dealloying

A difference in chemical potential between the elements in a homogeneous alloy can lead to selective etching of the less noble component(s) and the formation of a porous structure of remaining more noble component(s). The dealloying technique has been widely exploited in numerous synthesis processes[42], for example, in the fabrication of high surface area NP electrodes [43, 44] and NP gold nanowires [45, 46]

1.3.1.2.1 Critical Potential

As suggested by several researchers [21, 22, 25, 36, 47, 48], the selective dissolution of an alloy fails to occur under a characteristic voltage called critical potential, even if all other favorable conditions/parameters are met. Critical potential is important in a way that it is a unique system parameter depending on both extensive criteria (alloy and electrolyte composition) and intrinsic criteria (potential and scan rate) [36, 47] to characterize the level of readiness of an alloy for possible selective dissolution. The characteristic voltage is conventionally defined [49] as the onset of dealloying process which features an abrupt increase of the current density in a typical voltammetry plot (see Fig 1.2). There are difficulties in determining the characteristic voltage experimentally [21, 22, 36, 47, 48], so alternative methods have to be used instead. Typically, two ways have been used to quantify the characteristic voltage: the first one involves the extrapolation of slope in the ‘passivation-like’ region along with the slope of the abrupt rising current region [47, 49]; the second one is to pick a preset threshold of current density (generally picked around knee point region) and get the corresponding voltage reaching this threshold [36, 47]. In this work, the first method is chosen with minor modification: on the vicinity of smooth knee point for characteristic voltage, three tangent lines could be drawn (one on ‘passivation-like’ region, one on almost-linear-ramp region, and the third one in between). As a result, two characteristic voltage points form by intersection of the extrapolation of those three tangent lines. The

lower intersection voltage was chosen as representative characteristic voltage all through the work.

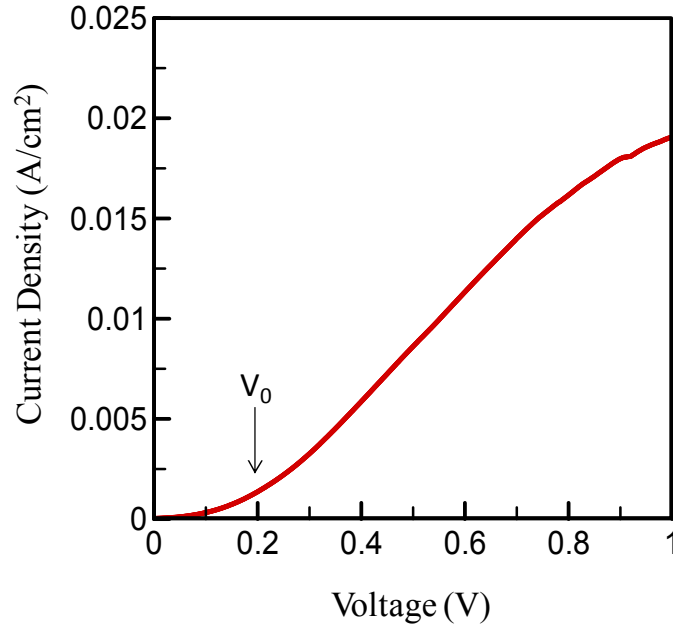


Figure 1.2 One example curve of current density as a function of applied voltage during dealloying

1.3.1.2.2 Dealloying Mechanism

Several models have been proposed explaining the selective dissolution process resulting in a porous dealloyed layer with a certain ligament/pore size. Two fundamental questions to be asked are: (1) where does dealloying initiate and (2) what the transportation mechanism is that enables the alloy-electrolyte interface to propagate and dissolve more of the less noble element.

Forty et al. [10, 32, 33] published a series of papers from 1960s to 80s proposing a mechanism known as terrace-ledge-kink model of dissolution of less noble A atoms from a A-B alloy as shown in Fig. 1.3. By ignoring molecular adsorption, oxidation and complexing effects associated with electrolyte, and assume dissolution involves only ionization and solvation of metal atoms. Forty proposed that dissolution should be firstly initiated in the kink sites (K) where atoms are least firmly bounded. The dealloying

current now will be dominantly composed of A atoms. As time goes by, the kink site on the free surface will hence gradually be occupied by noble B atoms and the dealloying current should diminish. Thereafter, the depletion of A atoms at kink sites forces the dissolution proceed only at non-kink sites (N) or terrace sites (T), which generally requires greater activation energy or overpotential. Eventually, without any transportation of fresh A atoms, all the surface sites are occupied by the more noble B atoms and dealloying should come to a halt. The results thus infers that atom transportation transport mechanism by virtue of which the atoms of the less noble metal A reach the surface and atoms of the more noble metal B aggregate is a must in the dealloying process.

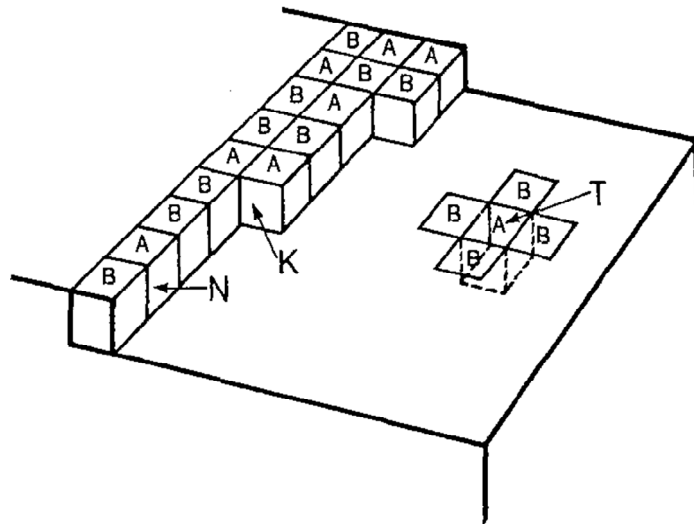


Figure 1.3 Schematic representation on an atomic scale of the surface of an alloy composed of dissolvable A atoms and noble B atoms. K is a kink site on surface step; N is a non-kink site on a step; T is a terrace site.[32]

Pickering et al. [17, 38] discussed this important issue in detail in their work, proposing that one or more of three mechanisms operate: (i) Dissolution-Redeposition mechanism: both metals ionize followed by redeposition of the more noble metal; (2) Surface Diffusion Mechanism: only the less noble atoms dissolve and the more noble atoms aggregate by surface diffusion; (3) Volume Diffusion mechanism: only the less

noble atoms ionize and enter the solution and atoms of both metals transport in the solid phase by volume diffusion.

Sieradzki et.al [50, 51] proposed a mechanism based upon percolation theory. They found that when dissolution of the less noble element is permitted from highly coordinated (terrace) sites, the dealloying threshold is found to be close to the conventional site percolation threshold for the structure. Sieradzki suggesting that there exist continuous connected clusters of the less noble element within the solid solution of the alloy to facilitate fresh less noble atoms transferring to surface as well as electrolyte penetrating deep inside.

A more recent numerical study is done by Erlebacher et al. [26, 48, 52] presenting how the competition between dissolution of less noble element and agglomeration of the more noble one can lead to an interconnected network of struts. The authors describe a process that starts with the dissolution of a single Ag atom of close-packed (111) orientation, leaving behind a terrace vacancy. The silver atom coordinating this vacancy is then the next one to be dissolved as it has lower activation energy comparing its counterparts, which in turn get a chain reaction of stripping the entire terrace. Au adatoms diffuse and condense to form gold-rich clusters droved by an extremely strong driving force. When the next layer is attacked by electrolyte, more gold adatoms are released onto the surface and diffuse to the gold clusters left over from dissolution of previous layers, further expose fresh layer to attack by electrolyte. These gold clusters in a 3D view are mounds with gold-rich tops and that have alloy composition on the bottom (belonging to the unattacked alloy layer). Note that these mounds could be undercut during the process. Ultimately, this leads to pit formation and porosity. The mode described here starts with an idealized surface with no roughness and no irregularities. Such defects can profoundly affect the manner of dealloying.

1.3.2 Mechanical Properties of NP Metal Foams

NP metal foams have a variety of distinct characteristics that set them apart from both bulk metal foams and other nanostructured metals (e.g. abundance of surfaces and similar characteristic length scales for the geometrical constituents and grains). These characteristics affect deformation mechanisms in NP metal foams and their overall mechanical behavior in unexpected ways by coupling, for example, mechanical response with other fields such as chemical/electric/thermal [4, 53, 54].

The mechanical robustness of nanoporous systems is an important consideration in applications. The abundance of surface area in NP metal foams is expected to affect both stiffness and strength. Experimental observations [55-57] and theoretical work [58, 59] have monitored the tendency of NP Au ligaments to deform while undergoing surface relaxation. The existence of the surface has in turn allowed NP metal foams to actuate under external stimuli by changing (increasing/decreasing) sample dimensions [56, 57, 60]. This behavior is thought to arise from the high surface to volume ratio. In polycrystalline NP metal foams grains within the struts are bounded by grain boundaries and free surfaces. This high amount of constraint due to the free surface, its interaction with the grains within the struts is expected to further influence mechanical behavior.

Microscopically brittle as the NP material is [8, 30, 61], traditional mechanical test methods such as microtensile or microbending experiments turns out to be difficult [62]. Instead, experimental testing of NP materials are usually carried out by Nanoindentation Tests [61, 63-65] and Micropillar Compression Tests [62, 66].

To date, the majority of mechanical property investigations of NP metal foams have centered on the change relative density (Gibson-Ashby scaling law) and ligament size (size effect) [31, 63, 64, 67-71]. The dependence of strength on the ligament network geometry has been confirmed in bulk metal foams but rarely reported in NP metal foams. The following text will provide a brief review on each of the above mentioned topics.

1.3.2.1 Gibson-Ashby Scaling Laws

As Gibson and Ashby mentioned in their book [72], for macroscale porous materials, there exists a scaling law of yield strength and effective macroscopic Young's modulus which governed by corresponding properties of its solid bulk counterpart and relative density.

$$\sigma_y = C_1 \sigma_B (\rho_{NP} / \rho_B)^n \quad (1.1)$$

$$E = C_2 E_B (\rho_{NP} / \rho_B)^n \quad (1.2)$$

Where σ_B and ρ_B are the yield strength and density of the massive samples of the solid bulk phase, and ρ_{NP} is the density of the porous counterpart. ρ_{NP} / ρ_B is termed relative density of porous materials. C_i and n are empirical constants.

Even though the scaling equations was originally intended to account for the properties of cellular material with ligament/pore size typically 100 μm or larger, and as we will see later that due to the nanoscale of pore size and high strength of ligaments the calculated yield strength by scaling law has distinct deviation from the real value, Gibson-Ashby Scaling Law still serves as a good starting point to give us qualitative inspection on nanoporous materials behavior.

1.3.2.2 Size Effect

A variety of NP foam ligament and pore size could be achieved by varying dealloying conditions and post-dealloying heat treatment process. Ligament and pore size is reported to be controlled by initial precursor alloy composition and synthesis parameters [41], applied dealloying potential [31, 73] as well as dealloying temperature [35]. It is also reported that post-dealloying processes such as subsequent annealing [8, 12, 63] or immersion into an electrolyte [5] can effectively coarsen the ligament diameter and increase the pore size.

Yield strength is defined as the stress at which a material elastic deformation ends and plastic deformation takes over. From Gibson-Ashby Scaling Law, the yield strength of NP metal is governed by yield strength of the bulk counterpart and the relative density. However, numerous study has shown that the measured strength of the NP metal is significantly higher than what predicted by Scaling Law [31, 35, 62, 63, 74, 75]. Some reports show that it is even stronger than their bulk counterparts [63]. It was found that strength of nanoscale ligaments is very high when inversely calculated by Scaling Law [31, 63, 74, 75], which goes in accordance with the recent nanoscale studies that nanorods and nanowires also exhibit a remarkably higher yield stress than their bulk metals [66, 68, 69].

Nanoindentation test is used by several researchers (Hakamada et al. [63] and Biener et al. [30, 31], etc.) to acquire corresponding yield strength data. In the indentation test of porous metal, with relative densities $\sim 4\%$, the plastic poisson's ratio tends to be ~ 0 . As a result the deformation proceeds via gradual densification and is predominately confined in the contact region [14] (i.e. the surrounding material does not constrain the deformation [63]), hence, the yield strength is equal to hardness H (rather than the famous triple relation), which was directly read out from nanoindentation experiments [72, 76]. While there are no measurements of the plastic poisson's ratio in NP metal foams, we anticipate that due to the high relative density values it is greater than 0. Experimental observations of nanoindentation in NP metals show that a decrease in ligament size will increase in the yield stress, and the yield stress of the nanosized Au ligament was much higher than that of bulk polycrystalline gold yield stress[30, 31]. In simple word, the results could be summarized as "smaller is stronger". Biener et al. [31] also pointed out that the ultimate strength in nanoporous metals can be reached when the ligaments attain the theoretical strength. This results is further confirmed using Micropillar compression technique by Volkert et al. [62], who observed the yield strength of submicron Au columns follows the power law d^{-n} , where d is the column diameter and

n is 0.6 by curve fitting. The reason for experimentally observed size dependence is most convincingly explained by dislocation source limited deformation [31, 62, 77, 78]. The smaller the ligament is, the higher the applied stress required activating the dislocation sources and hence the higher initiate yield is until the theoretical shear strength is reached (about 10 nm of ligament size). It is also suggests that decreasing the feature size beyond this point will not further increasing its strength but rather weaken the material, which is similar to the reverse Hall-Petch regime predicted for nanocrystalline materials [31].

With all the above mentioned aspects, we have seen that nanoporous material acts differently from the porous material with large pores. The Gibson-Ashby Scaling Law should be revised to take size effect into consideration [14, 31].

Elastic property drew less attention comparing to strength for NP material, and there still exist a controversy in publication on whether Gibson-Ashby Scaling Laws precisely predicts the values, and on whether size effect rules in the elastic properties.

Several studies [61, 62, 64, 65] report Young's modulus values in the case of NP Au in the range of 5-13 GPa with relative densities ranging from 25 to 40% [34] by micropillar compression test as well as sharp tip nanoindentation go in good agreement with the modulus of 7-11 GPa predicted by the scaling laws using a relative density of 36% and Young's modulus of single crystal Au of 57–85 GPa [62]. Also, they are in favor of the sample size effect to be negligible on Young's modulus at the length scales studied.

Mathur et al. [71] however, report a dramatic rise in the effective Young's modulus of NP-Au with decreasing ligament size (especially below 10 nm) which is similar to the case of yield strength. The method they are using is called "buckling-based method", which assumes that the NP thin film would buckle in a smooth sinusoidal waveform of the buckles, yielding a relation between critical buckling wavelength λ with film thickness h , the elastic moduli E and Poisson's ratios ν . They propose that the cause of the described size effect lies in a combination of factors that include density increase,

rise in surface stress effects, and higher bending stiffness owing to microstructural aspects.

A more recent study conducted by Hodge et al.[34] confirms the non-dependence relation of Young's modulus to sample size, but the effect of the relative density on the elastic properties of NP Au is observed to be much stronger than predicted by the Gibson and Ashby Scaling law. The authors suggest equation 1.2 only valid in the limit of low relative densities (pore diameter much larger the ligament size) where foam primarily deforms via ligament bending; for higher densities, contributions from ligament compression and extension should be taken into consideration.

1.3.2.3 Geometrical Effects on Bulk Metal Foams

Even though rarely reported in NP materials, effect of cell morphology on bulk metal foams has been confirmed by a list of publications [79-84]. Nieh et al. showed in their work [81] that the elastic collapse stress (yield stress) of open-cell aluminum foams in the longitudinal direction is higher than that in the transverse direction. Wang et al. [79, 80] systematically compared effective moduli and initial yield strengths of a variety of periodic cell structures under in-plane loading and 3D triaxial loading with different unit cell geometry. By tailoring porous morphology from strip-shaped to spherical-shaped, Jiang et al. increased compressive strength by a significant amount [82]. It was found that density is the primary variable controlling the modulus and yield strength of foams while the effects of other variables such as cell size and shape could also make a difference.

1.4 Thesis Organization

This section describes how the thesis will be organized in the following four chapters.

Chapter 2 will describe the transversely isotropic morphology of NP Pt foam that can be obtained through varying electrochemical parameters. The rate of progression of the

dealloying front is correlated to the observed current-time plot and a phenomenological model is derived.

Chapter 3 presents an experimental examination to understand the choice of initiation sites on the free surface of the amorphous alloy.

Chapter 4 presents the mechanical properties of various NP metal foams using nanoindentation. Different analytical models are derived to rationalize the experimental measurements.

The final chapter summarizes all results and presents recommendations for future work.

CHAPTER 2

SYNTHESIS OF TRANSVERSELY ISOTROPIC NANOPOROUS PLATINUM

Part of this chapter is based on the following accepted paper:

Y. Li, A. Antoniou, *Synthesis of transversely isotropic nanoporous platinum*, Scripta Materialia, 2011

Abstract

We examine the influence of electrochemical parameters on transversely isotropic nanoporous (NP) platinum foam synthesized from amorphous Pt_xSi_{1-x} by dealloying. The externally applied potential controls the size of the Voronoi polyhedra on the free surface with sizes ranging from 0.01-0.35 μm^2 . The shape of the amperometric curve is governed by the dealloying front progression that in turn advances faster than the rate of diffusion of Si in the electrolyte.

Keywords: nanoporous, metal, foam, amorphous, corrosion

2.1 Introduction

Nanoporous (NP) metal foams combine desirable characteristics of metals with unique nanoarchitectural features to yield weight normalized properties far superior than either dense metals or bulk metal foams. Due to their high surface to volume ratios these structures show great promise as components of fuel cells [1, 32], as sensors and have been suggested for use in biological applications, for example as antimicrobial scaffolds [2] or platforms on which to explore biological material behavior [3]. NP metal foams

are synthesized by dealloying: whereby the less noble element(s) in an alloy is (are) selectively dissolved in the electrolyte leaving behind the more noble element(s) to self assemble in a three dimensional network of structures [2, 8, 10, 26, 32, 41]. This controlled corrosion technique consistently produces struts and pores with the same range of dimensions [8, 10, 15, 23-25]. Most commonly, *isotropic* open cell NP foam has been synthesized but anisotropic structures have also been reported [19, 20, 41]. Anisotropy is manifested by either preserving features of the pre-cursor alloy after dealloying (such as grain boundaries) or by preferentially dissolving the sacrificial element from select sites on the free surface. The latter synthesis technique has so far only been observed when the initial alloy is amorphous [3, 41]. In the work presented here, we report on the degree of control one can have during synthesis of transversely isotropic foam assembled during dealloying. An example of such a structure can be seen in Fig.2.1. The study can be important in understanding how the surface of amorphous alloys can be further modified to potentially improve their functionality and biocompatibility [85].

Table 2.1 A summary of sample parameters before dealloying

Sample	Substrate bias voltage (V)	Initial composition
A	0	Pt _{0.33} Si _{0.67}
B	300	Pt _{0.37} Si _{0.63}

2.2 Experimental Methodology

The NP Pt samples used in the present study were made by electrochemical dealloying or etching of Pt_xSi_{1-x} amorphous alloys. As described in Table 2.1, two amorphous Pt_xSi_{1-x} alloy thin films with composition of x=0.33, 0.37 were deposited by

magnetron sputtering under different bias (0, 300V). The co-sputtered films were deposited on Si (100) substrates at room temperature. For better adhesion, a thin Ti layer ($\sim 20\text{\AA}$) was deposited on the Si substrate prior to the co-deposition of the amorphous $\text{Pt}_x\text{Si}_{1-x}$ thin films. X-ray diffraction (XRD) and transmission electron microscopy (TEM) were carried out to verify the amorphous state of the thin films. The composition of the amorphous films was further determined by Rutherford Backscattering Spectrometry (RBS) [86].

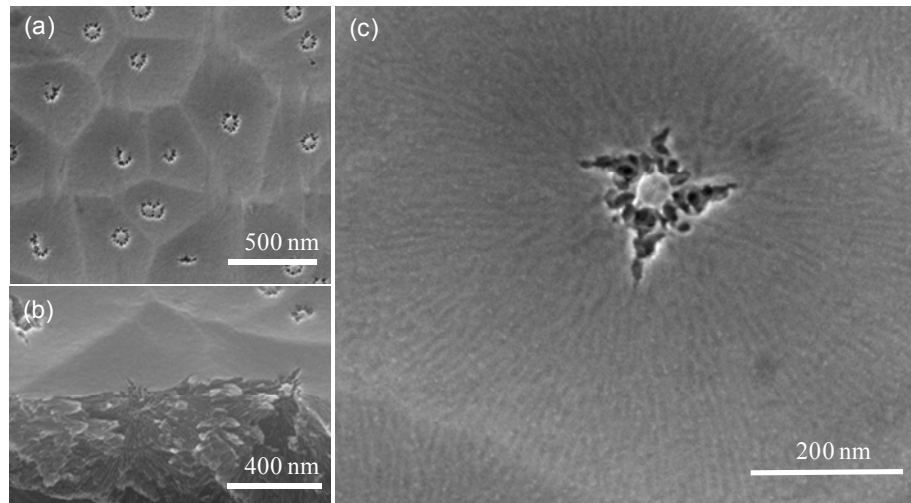


Figure 2.1 SEM (a) plan and (b) 52° tilt views of Voronoi type nanoporous platinum foam with 0.7V dealloying voltage and 200s dealloying period, (c) plan view image of the radial-like strut of Voronoi-type NP Pt foam

Electrochemical experiments were carried out in a conventional three-electrode cell, with Pt counter electrode and calomel reference electrode, using an electrochemical analyzer/workstation (Model 700D, CH Instrument). Samples with working area around 5mm^2 were coated with thin polymer layer on the backside to prevent substrate exposure in the solution. The electrolyte of 3 % (by vol.) hydrofluoric acid (HF) in Nanopure water was freshly prepared and all experiments were conducted at room temperature.

A linear sweep voltammetry (LSV) was first applied with scan rate of 3 mV/s. Figure 2.2(a) presents a typical voltammetry diagram for Sample Set A. The voltammetry curve follows a sigmoid shape which starts comparatively flat and then increases sharply around certain critical potential (denoted as E_0) before it finally reaches a plateau. Besides LSV, several representative dealloying potentials (0.3, 0.5, 0.6, 0.7, 0.9V) were selected and samples were dealloyed at a constant potential for a set amount of time. After electrochemical dealloying, the samples were immediately rinsed with distilled water and air-dried afterwards.

The critical potential (E_0) is an important system parameter that defines the onset of dealloying [49]. Below this value, selective dissolution of an alloy fails to occur even if all other favorable conditions/parameters are met [21, 22, 25, 36, 47, 48]. The critical potential depends on both extensive quantities such as alloy and electrolyte composition and intrinsic quantities such as potential scan rate [36, 47]. Hence, one can use this parameter to scale against differences in alloy composition or scan rates. In this work the critical potential is defined by extrapolating the slope of the abrupt rising current along with the slope in the ‘plateau’ or ‘passivation-like’ region [47, 49]. The critical potentials for both sample sets are $E_0^A = 0.15V$ and $E_0^B = 0.11V$ respectively.

The overall surface morphology of the amorphous and dealloyed samples was inspected by a Zeiss Ultra60 Scanning Electron Microscope (SEM). The evolution of the synthesized Voronoi polyhedra on the free surface was investigated by performing interrupted dealloying experiments and monitoring the same sample region through SEM. Additional measurements of features of interest were performed using the open source, Java based, image processing package, ImageJ [87].

2.3 Results and Discussion

Figures 2.1 (a), (b) and (c) present the resulting NP-Pt foam structure that highlights two sub-structures with distinct scales of anisotropy [41]. The first level of anisotropy is a pattern featuring concave hyperstructures resembling Voronoi tessellation on the free surface as shown in Fig. 2.1 (a). The second level of anisotropy lies underneath the above mentioned hyperstructures, in which Pt foam with nano-sized ligaments forms as a result of dealloying process as shown in Figs. 2.1 (b) and (c) [41]. These ligaments are elongated and emanate in radial direction from a unique point on the free surface. TEM verified that NP Pt is polycrystalline with 5 nm size grains. The ligament size was found to be ~60 nm in length and 10 nm in diameter along the radial direction.

In this work, we examine the effect of electrochemical parameters on the synthesis of transversely isotropic structures and examine how the current density relates to the dealloying front evolution. Figure 2.2 (b) shows a plot of the current density as a function of time for different applied voltages (0.3, 0.5, 0.7 and 0.9 V) during dealloying. Previous work [86] has demonstrated that in the case of the amorphous $\text{Pt}_x\text{Si}_{1-x}$ system, the silicon volume fraction completely dissolves in the electrolyte and the Pt volume fraction remains behind to self-assemble into foam. Thus, the current density measured here is directly proportional to the amount of silicon removed during dealloying. As can be seen by the curves, for $E = 0.3\text{V}$, the potential nearest to the critical potential, very little current is measured and thus little dissolution occurs. This is verified by the SEM image, Fig. 2.2 (c), where the surface has undergone minimal change from the amorphous/undealloyed state. The above observation is consistent with other binary

alloy systems [25]. For $E = 0.6$ V the current density time plot increases linearly until it reaches a plateau after a characteristic time ($t_{ss} \sim 100$ s). The corresponding SEM image, Fig. 2.2 (d), shows the formation on the free surface of concave Voronoi polyhedra. As we showed in our previous work [41], each polyhedron consists of radially emitting nano-sized ligaments of Pt. As the dealloying voltage increases to $E = 0.7$ V, the current density approaches steady state at earlier time ($t_{ss} \sim 60$ s). The plateau itself occurs at a greater current density than $E = 0.6$ V indicating that more silicon dissolution has occurred. The SEM image, Fig. 2.2 (e) shows that more Voronoi polyhedra have formed on the free surface, with each polyhedron occupying a smaller in-plane area. Underneath the hyperstructure, the Pt morphology remains the same: the grains are still 5 nm in size, Ligaments size remain unaffected by the applied voltage. Finally, at $E = 0.9$ V, the current density as a function of time plot in Fig. 2.2 (b) shows that a higher steady state current value is attained at an earlier time than $E = 0.7$ V. The corresponding SEM image of the sample dealloyed at $E = 0.9$ V is shown on Fig. 2.2 (f). The Voronoi polyhedra are no longer visible on the free surface. The hyperstructure underneath no longer retains the radial/circumferential ligaments. In fact ligaments are vertically aligned in space, with grain size of 5 nm and same ligament size. The above trends apply for the initial alloy deposited under greater bias (Sample Set B). We note that the decrease of the pore size with increased applied voltage is similar to that observed during the synthesis of isotropic NP metal [41]. For this system, the ligament diameter on the other hand remains invariant to the externally applied potential.

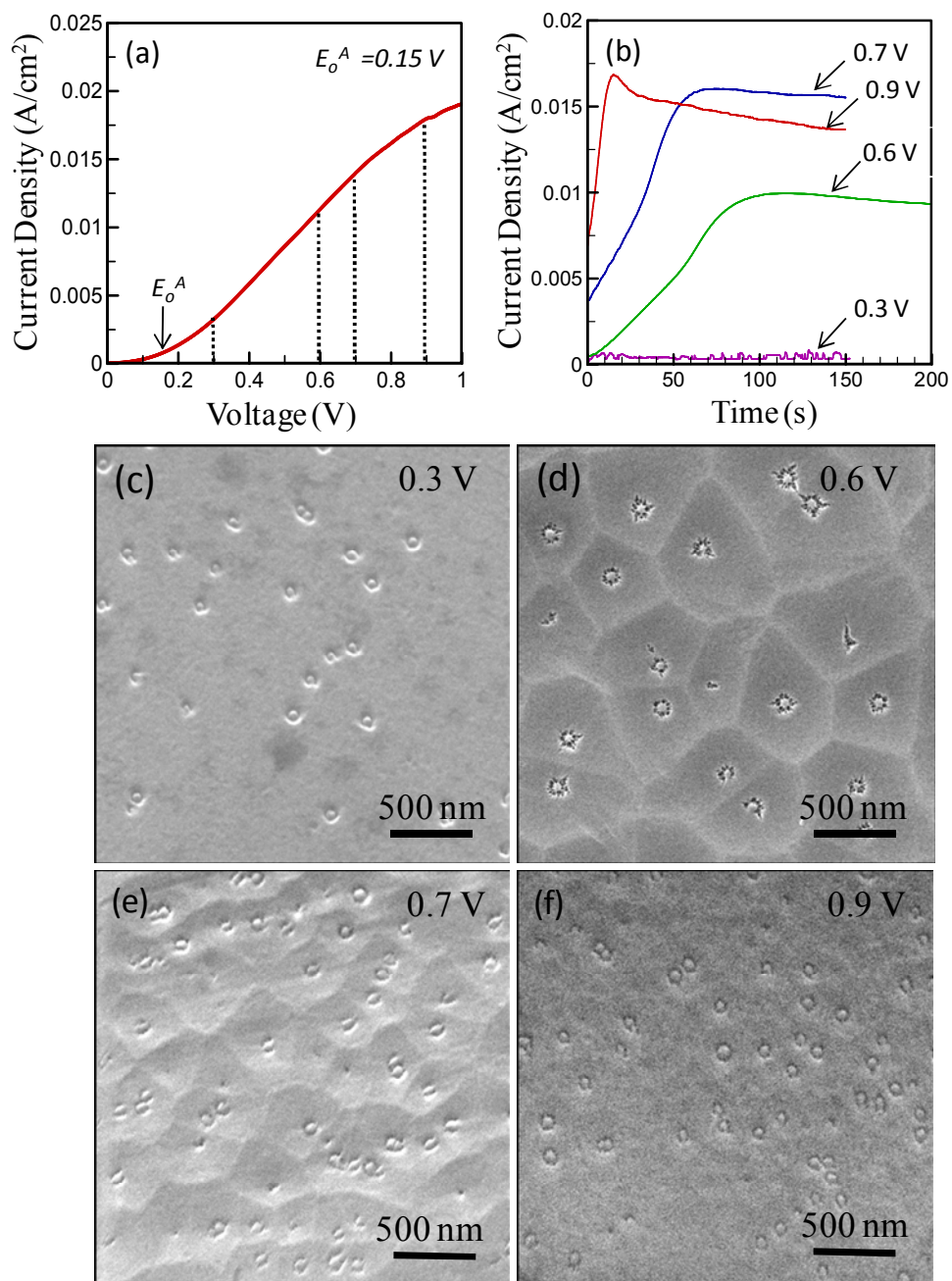


Figure 2.2 (a) Current density as a function of applied voltage during dealloying of Pt_{0.33}Si_{0.67} (Sample Set A). E_0 is the critical potential. (b) Current density as a function of time during dealloying of Pt_{0.33}Si_{0.67} with different dealloying voltages and the resulting plan view SEM image for: (c) 0.3V; (d) 0.6V; (e) 0.7V; (f) 0.9V.

From Fig. 2.2 we see that by increasing the externally applied voltage, the number of dealloying sites increases while the polyhedra size decreases. Figure 2.3 shows a plot of the normalized Voronoi polyhedra diameter as a function of normalized dealloying potential for both sample sets. The average polyhedron diameter, D_p is found from the average polygon area of each sample and is normalized to $D_0 = 5$ nm. This value roughly corresponds to a typical width of the initial flaw in Batch B as measured from Atomic Force Microscopy (AFM) scans of the initial alloy surface prior to dealloying. Even though pre-existing ~ 60 nm features are visible for Batch A, dealloying commences from a depression around the circumference of each feature with initially comparable size to D_0 , as seen in Figs. 2.1(a) and (b). The dealloying potential, E is normalized with the critical potential E_0 . The normalized potential scales differences in alloy composition or electrolyte concentration. For $E \sim E_0$, no Voronoi polyhedra form. For $E \sim 10E_0$ dealloying commences from enough sites on the free surface that Voronoi polyhedra no longer form. In essence, dealloying commences from almost anywhere on the free surface and propagates uniformly through the thickness. Based on the experimental observations the polyhedron size decreases with increasing dealloying potentials exponentially as follows:

$$D_p/D_0 = e^{\alpha(\frac{V}{V_0})+\beta} \quad (2.1)$$

For this particular system, the parameters are $\alpha = -2.28$ and $\beta = 4.64$ based on a fit with the experimental measurements. As explained previously, the polyhedron formation is bounded so that the largest and smallest polygon size possible for this system is around $0.35\mu\text{m}^2$ and $0.01\mu\text{m}^2$ respectfully.

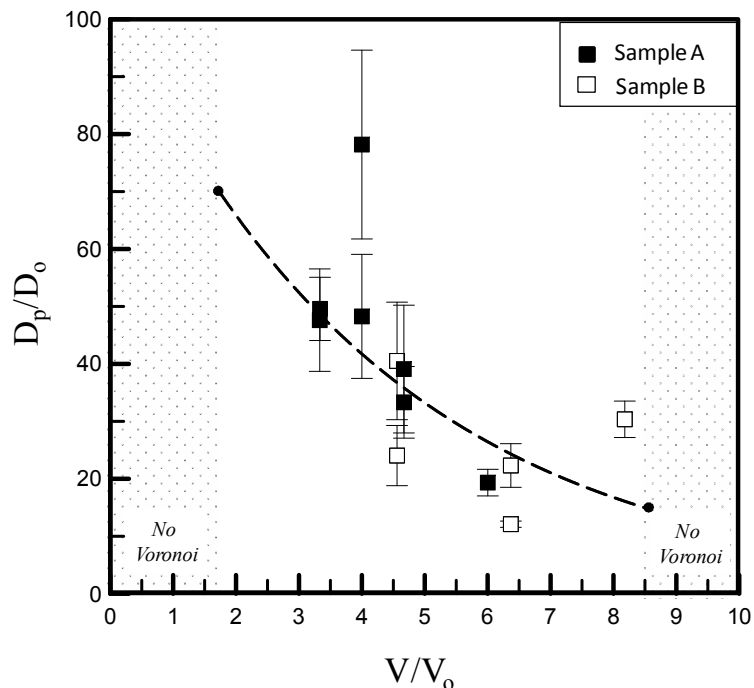


Figure 2.3 Normalized Voronoi polyhedral diameter as a function of normalized dealloying potential for both sample sets, where D_p is the well-established polyhedral diameter and $D_0=10$ nm. The dashed line is a simple data fit. The shaded regions mark where no Voronoi polyhedra can form.

For several binary alloy systems that can selectively dissolve and form NP structures, a parting limit exists i.e. a critical initial alloy composition above which selective dissolution is not possible. In the Pt_xSi_{1-x} system, we have shown [41] that isotropic open cell NP metal can result for compositions when the amount of Pt is between 10-35%. The conditions for synthesis of Voronoi polyhedra appear to be a bifurcation of selective dissolution. Instead of uniform dealloying from any site on the free surface, dealloying commences from select sites. As the externally applied voltage increases, more sites react with the electrolyte, until eventually all the free surface simultaneously interacts with the solution and uniform dealloying can occur. In our work we have examined the initiation sites and have found them to have greater roughness than

the surroundings (detailed in Chapter 3). Based on the above observations, we hypothesize that Voronoi polyhedra can form when the initial alloy is crystalline but presence of secondary phases, composition or grain boundaries may hinder the uniform growth of Voronoi polyhedra seen on the free surface when the precursor alloy is amorphous.

We monitor the progression of the dealloying front from sites of greater roughness by a series of interrupted experiments. At every dealloying step we examine the evolution and NP structure formation through SEM. Figure 2.4 (a) shows the free surface of the initial alloy. Figure 2.4 (a) shows specimens from Sample Set A (Table 1) that have sites of large roughness and help identify the front progression. For every segment, an amperometry study was performed with $E = 0.5 \text{ V}$. Figures 2.4 (b) and (c) show plan SEM images of the dealloying front at 60 and 120s respectively. From Figs. 2.4 (a), (b) and (c) dealloying initiates and progresses in a radial fashion through the sample thickness and along sample surface. As the dealloying front comes into contact with the initial amorphous alloy, Si dissolves and Pt assembles into nanosized ligaments. Due to the dissolution of silicon, a dimensional change occurs that causes the formation of a depression (well) on the free surface. At the intersection of two dealloying fronts the boundaries of the Voronoi polyhedra form. We used the initiation sites on Figs. 2.4 (b) and (c) as the random sites for the mathematical prediction of the Voronoi boundaries calculated from Matlab. We have superimposed the prediction of the boundaries on the SEM image at $t=120\text{s}$. The composite image of the mathematical prediction is shown on Fig. 2.4 (d), which has very good agreement with the actual boundaries seen in SEM images. At the boundary intercept, the last amount of Si on the free surface dissolves into

the electrolyte and NP metal foam forms. From that point onward the dealloying front proceeds through the sample thickness. A tilt 52° cross-section view of NP Pt foam shown in Fig. 2.4 (e) shows the formation of NP metal foam near the high roughness site (marked by arrows). Fig. 2.4 (e) also shows the formation of a well (depression) due to the dissolution of Si.

The rate of dealloying front progression is examined from the sequential experiments. The front commences from sites of greater roughness and progresses in a semi-spherical fashion through the thickness and across the free surface until it encounters and overlaps with adjacent fronts. From that point onward, the front will dealloy only through the thickness direction. A schematic on Fig. 2.5 (a) shows a three dimensional view of the progressing spherical half-shell that is the dealloying front. Figure 2.5 (b) shows a 2D cross-section (A-A) of the dealloying front through the thickness. After two fronts intercept ($t > t_{ss}$) then dealloying progresses only through the thickness. We will focus on the initial front progression and its relation to the macroscopically measured current density. As we explained earlier, at the interface of the dealloying front with the electrolyte, Si will dissolve. In turn, Si dissolution is directly proportional to the current density measurements seen on Fig. 2.2 (b).

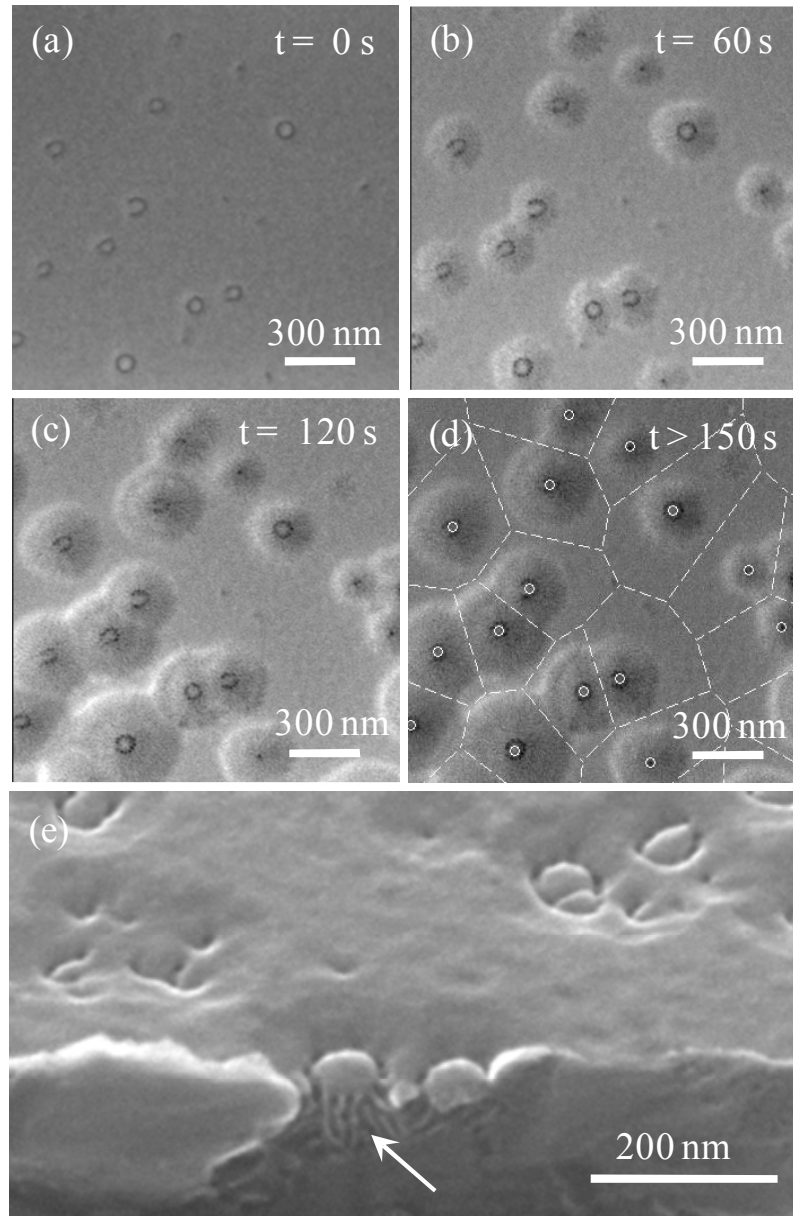


Figure 2.4 (a) Plan view SEM of the same region monitored at (a) $t=0$ s, (b) $t=60$ s, (c) $t=120$ s during dealloying at $E = 0.5$ V. (d) Mathematical prediction ($t > 150$ s) of the polyhedra boundaries using the initiation sites as input. Prediction is superimposed on the plan view SEM image obtained at $t = 120$ s (e) 52° tilt cross-section view near a dealloying site. White arrow marks the location where NP Pt foam has formed.

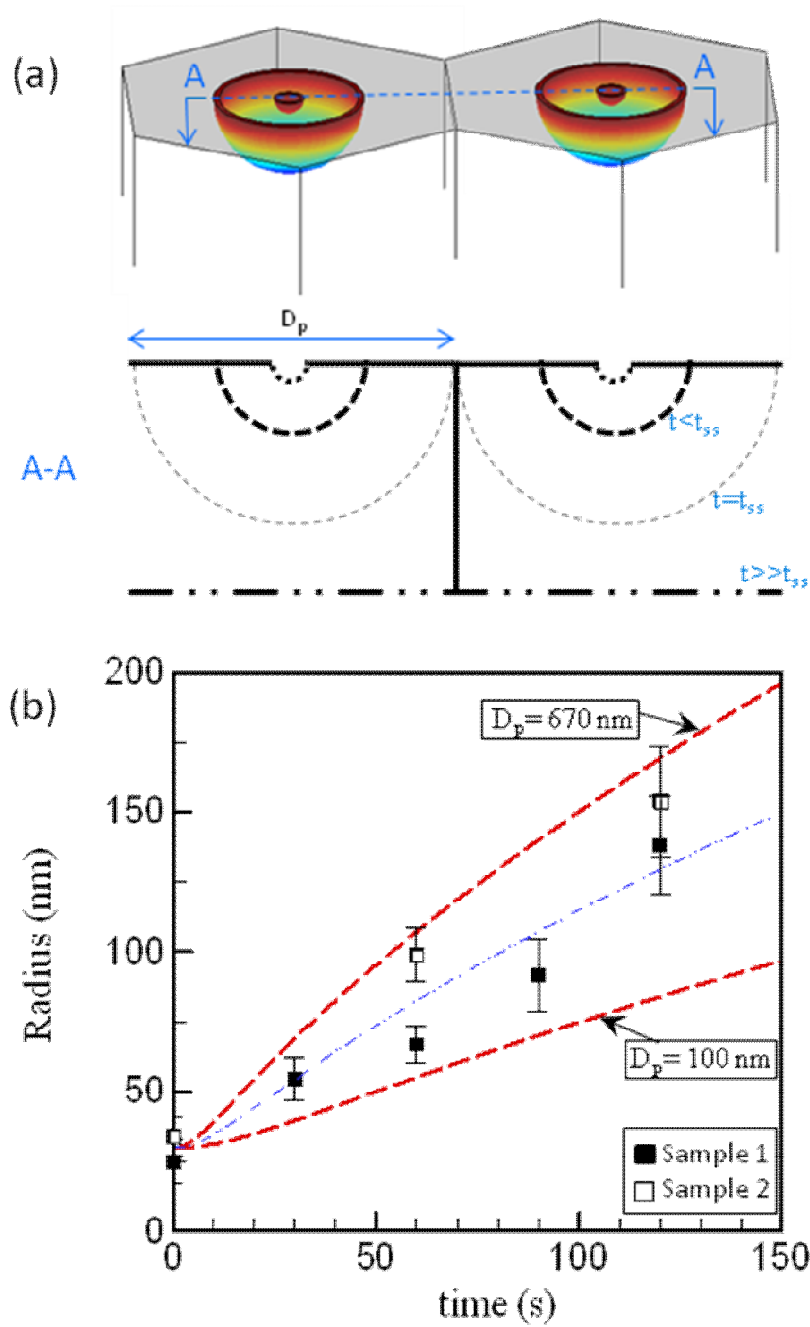


Figure 2.5 (a) Schematic 3-D and cross section views for the dealloying front progression at different time intervals. (b) Experimental measurements of dealloying front radius as a function of time for two different samples in Sample Set A. The red dash lines represent the phenomenological model predictions for the largest (670nm) and smallest (100nm) possible polygon dimensions.

We define the flux (J), of Si atoms dissolved in the electrolyte for a finite amount of time per unit area. At a particular instance in time, a finite volume of the amorphous alloy will be exposed to the electrolyte. We assume that dissolution of Si occurs only in the finite volume exposed in the electrolyte. For this system, the finite volume is a spherical half-shell of radius (r) that has finite thickness (as seen in Fig. 2.5 (a)). The radius of the half-shell increases in size with time. The flux of silicon atoms will relate to the exposed spherical half shell that grows with time as:

$$J = \frac{dr}{dt} 2\pi r^2 \quad (2.2)$$

The flux of Si ions dissolved in the electrolyte will also relate to the macroscopic measurements of the current density. Close inspection of Fig. 2.2 (b) shows that the current density is directly proportional with time until it achieves a steady state at time t_{ss} . In the first stage when $t < t_{ss}$, the current density linearly varies with time and thus J , the flux, will also be directly proportional with time,

$$J = Kt \quad (2.3)$$

where K is proportionality constant. From our experimental observations the following boundary conditions are set: the dealloying front initiates at greater roughness sites i.e. $r(t=0)=D_o/2$; steady state time is achieved when the dealloying front moves from bi-directional dealloying to uni-directional, i.e. only through the thickness. The latter occurs when dealloying fronts merge and Voronoi polyhedra form at $r(t=t_{ss})=D_p/2$. By combining Eq. (2.2) and (2.3) and applying the above boundary conditions, the radius of the dealloying front is found to be:

$$r = \left\{ \left[(D_p/2)^3 - (D_o/2)^3 \right] \left(\frac{t}{t_{ss}} \right)^2 + (D_o/2)^3 \right\}^{1/3} \quad (2.4)$$

For $t > t_{ss}$ the current density achieves a steady state and therefore the flux is constant, non-dependent with time. Substituting into Eq. (2.2) and using the boundary condition, $r(t=t_{ss})=D_p/2$, to yield

$$r = \left[(D_p/2)^3 \frac{t}{t_{ss}} \right]^{1/3} \quad (2.5)$$

Eqs. (2.4) and (2.5) describe the evolution of the dealloying front radius as a function of time based on a simple phenomenological model. The model captures the current density versus time response seen on Fig. 2.2 (b) where the steady state time is directly proportional to the polygon size. Fig. 2.5 (b) shows the radius as a function of time for samples forming Voronoi polyhedra with the smallest (100 nm) and largest (670 nm) average polygon sizes seen in SEM images. The data points are the result of the average radius growth from two different interrupted dealloying experiments for Sample Set A (one such experiment is seen in Fig. 2.4). The experimental results agree well with the model prediction (blue line) for a sample with the same average polyhedron size as Fig. 2.4. Therefore, the local measurements from the interrupted experiment conform with the phenomenological model.

The current density shape is very much controlled by the dealloying front progression. Thus, the size of the synthesized Voronoi polyhedra can be measured directly from the current density measurements. Furthermore, the rate of growth of the dealloying front is proportional with $(t^{1/3}, t^{2/3})$ and is thus, not diffusion controlled. Silicon is completely removed from the alloy as verified from RBS and TEM measurements. Therefore, at the atomistic level, silicon dissolves in the electrolyte by diffusion. The fact that the dealloying front progresses at a faster rate signifies that there may be processes in the nanoscale or mesoscale that facilitate faster exposure of silicon in

the the electrolyte. Such processes may be the formation of nano-sized “cracks” or voids that can expose more of the initial alloy to the electrolyte. Even though a lot of work on modeling in the atomistic scale has been done for dealloying, further work is needed to examine dealloying mechanisms at greater scales.

2.4 Summary

In summary, we have examined the synthesis of transversely isotropic NP metal structures from an initial amorphous alloy. We demonstrated that the externally applied voltage can influence the size of the in-plane Voronoi polyhedra that form on the free surface and the current density curve relates to the dealloying front progression. We have derived a phenomenological model of the dealloying front progression that agrees well with experimental measurements. We have finally determined that the dealloying front itself progresses at a faster rate than the atomistic diffusion rate of silicon. The above observations are important in understanding the parameters needed to synthesize anisotropic structures that will have different properties than isotropic. The study is also helpful in examining the behavior of amorphous alloys in corrosive environments.

This work was performed, in part, at the Center for Integrated Nanotechnologies, a U.S. Department of Energy, Office of Basic Energy Sciences user facility at Los Alamos National Laboratory (Contract DE-AC52-06NA25396) and Sandia National Laboratories (Contract DE-AC04-94AL85000). The authors would like to thank J.K. Baldwin for help with the amorphous alloy deposition.

CHAPTER 3

EXAMINATION OF DEALLOYING INITIATION IN AN AMORPHOUS Pt_xSi_{1-x} ALLOY

Part of this chapter is based on the following paper in preparation:

Y. Li, A. Antoniou, *Examination of dealloying initiation in an amorphous Pt_xSi_{1-x} alloy*

Abstract

We examine the initiation of dealloying in an amorphous Pt_xSi_{1-x} alloy at compositions near the parting limit ($x \sim 0.4$) when exposed to an aqueous solution of HF. We observe that dealloying initiates from select sites at the free surface and proceeds in a semispherical front through the sample surface and thickness. Atomic Force Microscopy measurements reveal that the initiation sites have greater local roughness than the surroundings. As the externally applied voltage increases, dealloying commences from sites with even smaller local roughness.

Keywords: nanoporous, foam, amorphous, initiation, roughness

3.1 Introduction

As promising candidates for a variety of applications including actuators [41], capacitor [88-92] and catalysts [1, 93], nanoporous (NP) metal foams have become an increasingly popular subject of research in recent years. NP metals are synthesized by a controlled corrosion technique called electrochemical dealloying where the less noble element(s) in a homogeneous alloy is/are etched away and more noble element(s) survive(s) to diffuse and aggregate leading to the formation NP struts.

Central to the dealloying mechanism description is the issue of initiation/nucleation of porosity in the dealloying process. Several proposed mechanisms, such as terrace-ledge-kink model first introduced by Forty et al. [10, 32, 33] and adopted by others [48, 52], provides an atomistic view explaining that the dealloying is expected to occur preferentially from kink sites (surface defects) where atoms have fewer neighbors to be bound and are therefore more vulnerable for dissolution. In this work we examine experimentally, the initiation of dealloying in an amorphous alloy with greater portion of the noble element ($x \sim 0.4$) and closer to the parting limit. We've demonstrated in our previous work, the synthesis of transversely isotropic nanoporous (NP) platinum foam from amorphous Pt_xSi_{1-x} by electrochemical dealloying [55]. This demonstrated new type of NP Pt morphology has two types of anisotropy: the concave hyperstructure resembling Voronoi tessellation on the free surface and the radially aligned ligaments and pores centered on a unique point on the free surface. SEM images of interrupted experiments which unveil the evolution of this sophisticated porous structure suggest that preferential initiation of dealloying starts at preferential sites. In order to better understand the evolution of this transversely isotropic structure and to further control/manipulate NP foam morphologies we need to examine the initiation mechanism more closely.

3.2 Experimental Methodology

Sample compositions and preparation technique are consistent with what has been mentioned in the previous chapters. In this study, in order to examine conditions for preferential initiation we used Atomic Force Microscopy (AFM) to monitor the surface roughness of the amorphous alloy prior and during the first hundred seconds of dealloying.

In order to monitor the same region of interest, the sample surface was marked using Focused Ion Beam (FIB). The AFM was operated in the tapping mode with slow scan rate (less than 0.5Hz). Backside Al-coated AFM probes (μ -masch Co.) with typical probe tip radius 10 nm and full tip cone angle 40° were used in the experiment. Also, a variety of techniques (RBS, cross-section TEM and Energy-dispersive X-ray spectroscopy) were used to confirm composition homogeneity through thickness and in-plane [41].

3.3 Results and discussion

To identify the effect of surface roughness on preferential initiation of dealloying sites, we employ corresponding SEM and AFM scan on pre-allocated regions of interests. Figure 3.1 shows a sequence of images of the evolution of a particular region of interest in sample set A when dealloyed at 0.5V for 120s. As seen from the AFM image pair Fig.3.1 (c) / (d), round pre-existing feature have higher roughness when compared to their surroundings. For a closer examination, one can perform a cross-sectional cut analysis along a particular direction, for example, an O-O cut (denoted on image pair Fig.3.1 (a) / (b)) is carried out and the result is showing on Fig. 3.1(e). These sites serve as a majority of initiation sites in this particular Pt/Si system where Voronoi polyhedron form with them as the nuclei.

Figure 3.2 gives a more intuitive view of the morphology transformation shaped by dealloying process. The AFM scans clearly show that dissolution of silicon enables a dimensional change which causes the formation of a depression (well) on the free surface. Similar results are seen in Fig. 3.3, for a sample dealloyed for the same amount of time (120s) but with a higher dealloying voltage (0.7V). It is worthy to point out that the pre-existing feature is not the only type of feature around which dealloying initiates. The scans also show spots other than the pre-existing feature undergo preferential dealloying purely due to their high surface roughness. The arrows on Figs. 3.3 (a) and (c),

and the cross-sectional cut analysis in x-x and y-y direction show that this area is rougher when compared to the surroundings (see inserted image of Figs3. 4 (c) and (d)).

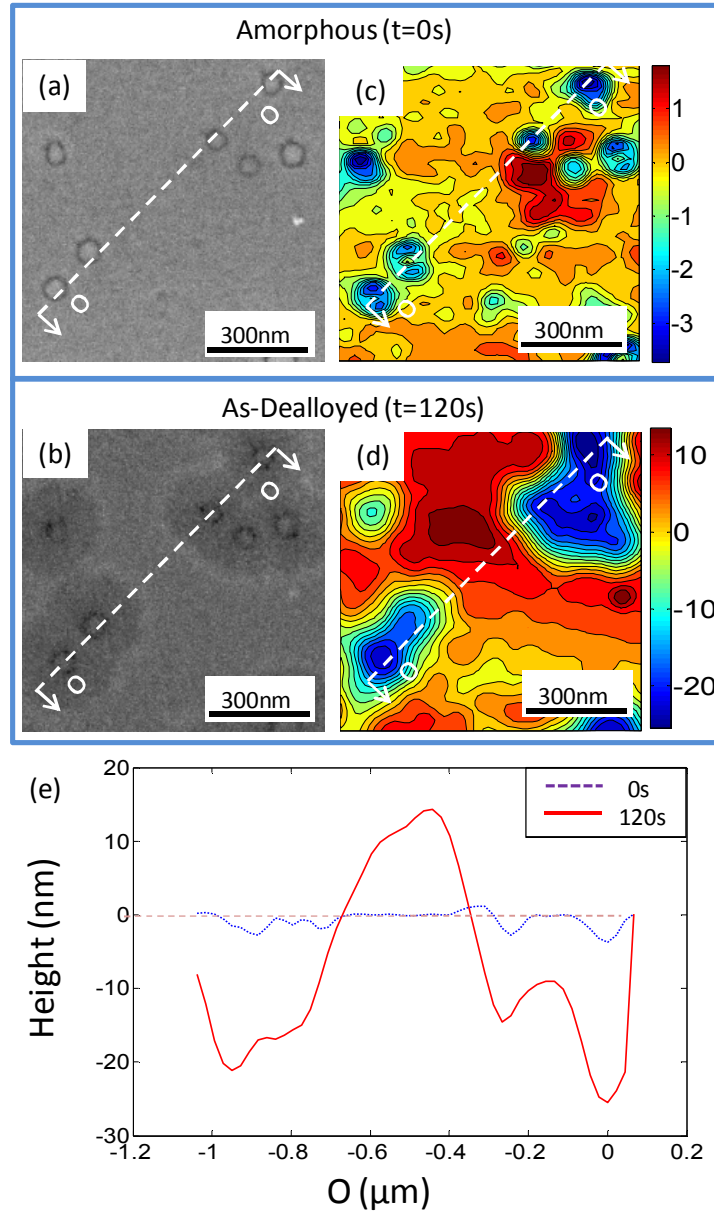


Figure 3.1 Amorphous state SEM (a) and AFM scan (c) and same region As-dealloyed (dealloying voltage 0.5V, 120s) SEM (b) and AFM scan (d). Surface roughness analysis of O-O cut (e), showing at a fixed voltage, dealloying initiate preferentially at high roughness spots.

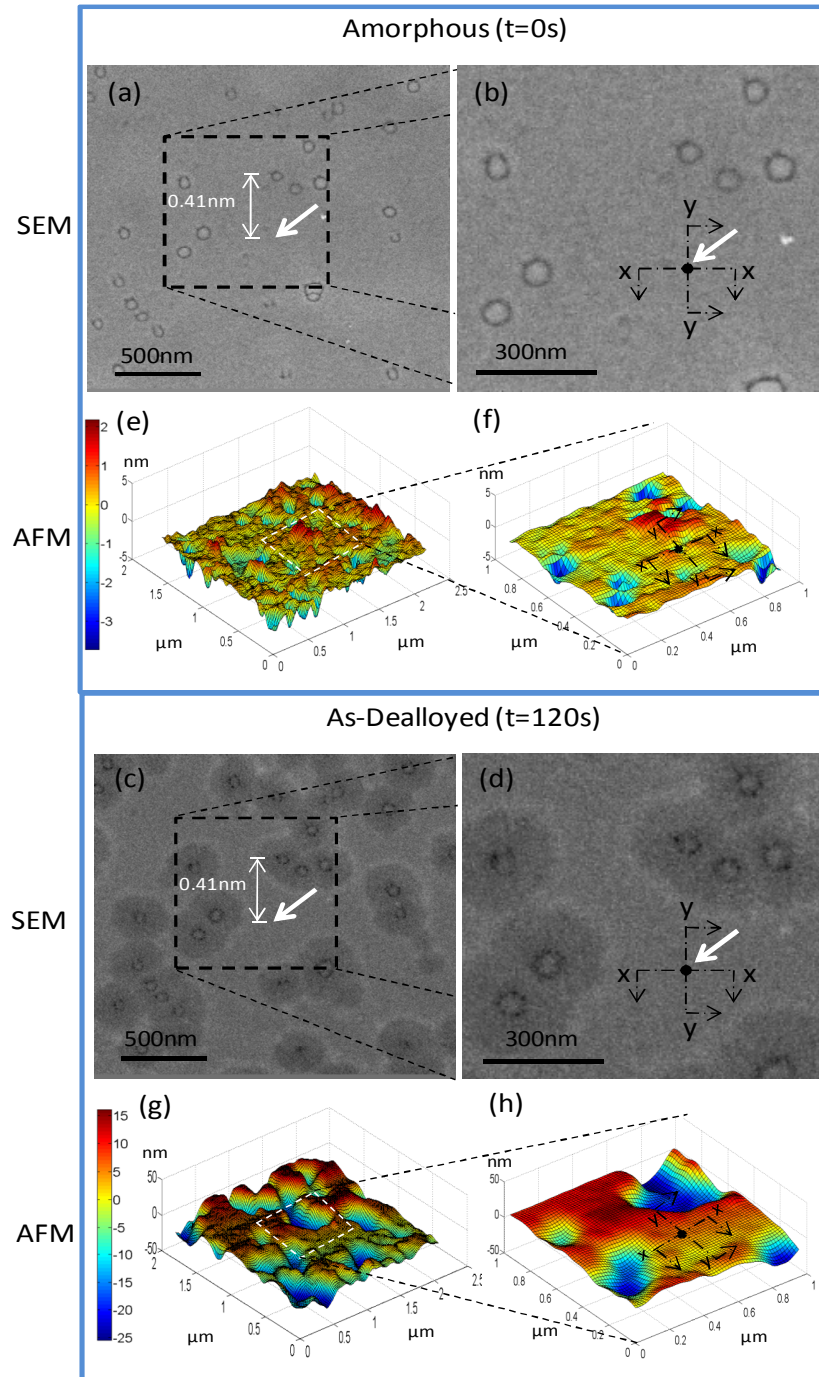


Figure 3.2 Images of a sample from sample set A dealloyed at 0.5V for 120s. Amorphous state (0s) SEM plan view (a) and its enlarged boxed area (b), corresponding location AFM scan image (e) and same enlarged boxed area (f). As-dealloyed (120s) state SEM plan view (c) and its enlarged boxed area (d), AFM scan image (g) and same enlarged boxed area (h)

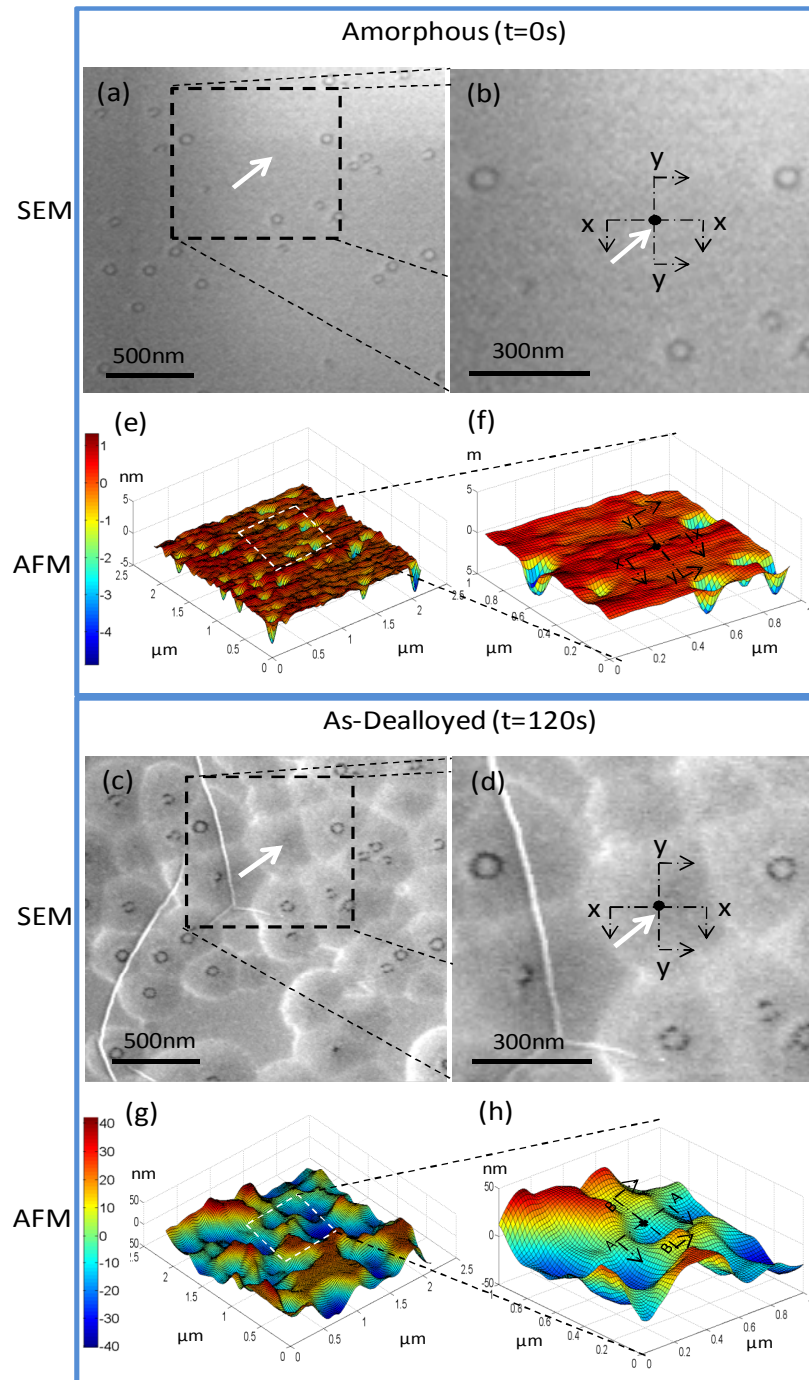


Figure 3.3 Images of a sample from sample set A dealloyed at 0.7V for 120s. Amorphous (0s) state SEM plan view (a) and its enlarged boxed area (b), corresponding location AFM scan image (e) and same enlarged boxed area (f). As-dealloyed (120s) state SEM plan view (c) and its enlarged boxed area (d), AFM scan image (g) and same enlarged boxed area (h)

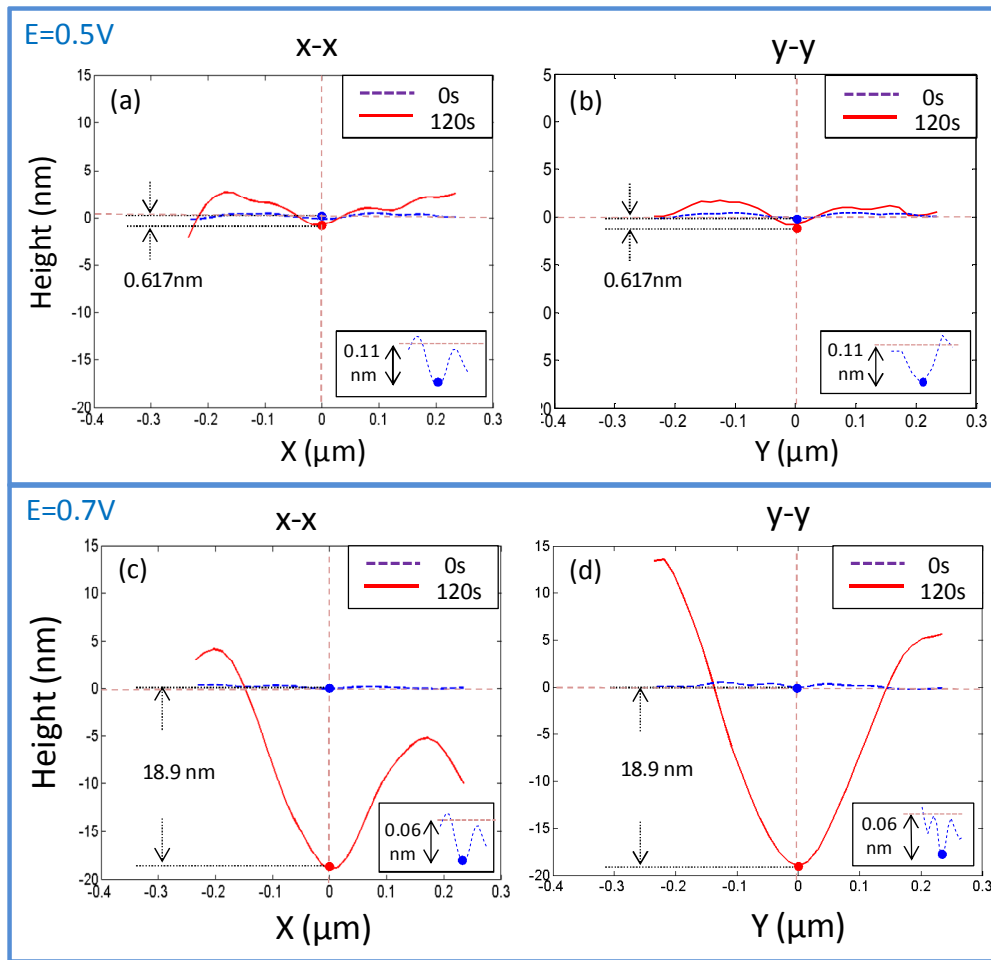


Figure 3.4 The upper images are x-x and y-y cut (referring to Figs. 3.2 and 3.3) surface roughness analysis for dealloying voltage 0.5V, the lower counterparts for 0.7V. Inserted images are the corresponding initial roughness.

The two figures demonstrate that at a given potential, dealloying commences at sites with greater local roughness. The density of initiation sites per area increases as the dealloying potential increases. We propose that there is a critical roughness value above which, dealloying can initiate. As the applied voltage increases, more and more sites are able to overcome this critical initiation condition.

If we approximate the greater roughness sites as nano-sized surface cracks we can draw parallels from fracture mechanics. They are defect sites similar to grain boundaries, and thus can allow for preferential dealloying to commence from these sites. The hardness of the amorphous alloys using instrumented nanoindentation were found to be H

= 9.3 GPa for Batch A and H=8.4 GPa for Batch B. This high hardness value is representative of brittle materials, i.e. materials with low fracture toughness. For similar silicide systems, fracture toughness is typically $\sim 1-5 \text{ MPa}\sqrt{m}$. Continuing with the analogy from fracture mechanics, the roughness of these sites is similar to the ‘crack’ length a . The initial film thickness is the overall sample width w and the externally applied potential changes the free energy of the system. While we cannot directly link the potential to a fracture toughness measure, we can say that the analogy allows to say that there are two parameters that control preferential dealloying in the system: surface roughness and dealloying potential. For same dealloying potential, instead of uniform dealloying from any site on the free surface, dealloying commences from select sites the surface with higher roughness (bigger a). These select sites will be easier to reach critical value and stand out from its peers to initiate dealloying. On the other hand, the higher the dealloying voltage (higher ‘ σ ’), the greater the number of surface points reach the critical value, thus more surface sites began to initiate depression.

3.4 Summary

In summary, based on the experimental observation and analysis, we confirm that dealloying initiates preferentially from sites of greater roughness in an amorphous binary alloy. By analyzing the effect of surface roughness and dealloying potential, we proposed a model with drawing an analogy to fracture mechanics to addressing the preferential initiation of dealloying. The system can serve as a model where the relationship between fracture toughness and dealloying potential can be derived. The properties of the initial alloy (roughness, strength, composition) still influence the resulting strength and geometrical arrangement of struts in the post-dealloyed NP structure.

CHAPTER 4

MECHANICAL BEHAVIOR OF TRANSVERSELY ISOTROPIC NP PLATINUM FOAM

Part of this chapter is based on the following paper in preparation:

Y. Li, A. Antoniou, *Mechanical behavior of transversely isotropic NP Platinum foam*

4.1 Introduction

Nanoporous (NP) metal foams with pores/ligaments size on the order of a few to tens of nanometers are attractive for a variety of applications. For example, their distinct nanosized foam morphology and highlighting character of large surface to volume ratio makes them ideal as components in fuel cells or batteries. Aside from energy applications, NP Pt foam with transversely isotropic features was recently found to be an ideal template for the study of diffusion mechanisms in lipid bilayer membranes [4]. In particular, morphologies with relatively small voronoi polyhedra were found to have superior performance i.e. enable faster diffusion of bilayer and greater fatigue life when compared to isotropic NP Au or Pt platforms. In this work we examine the mechanical behavior of Voronoi-type NP Pt using indentation to understand how their properties differ from those of isotropic structures.

The following sections describe the experimental methodology and results. Analytical predictions using linear beam theory are carried out to understand the origin of any strength enhancement.

4.2 Experimental Methodology

4.2.1. Sample preparation

Amorphous Pt/Si thin films with thickness around 1 μm were cosputtered on to Si (100) substrate. The thin films were then polymer coated on the back side (to protect Si layer) and dipped into 3% (by volume) HF dilute solutions to carry out electrochemical dealloying to selective dissolve Si in order to form nanoporous (np) Pt structures. The dealloying process at certain predetermined dealloying potential is performed using electrochemical analyzer/workstation (CH Instrument) at room temperature with traditional three electrodes setup where Pt serves as counter electrode and calomel as reference electrode. A series of predetermined dealloying voltage was chosen with reference to critical dealloying potential V_0 in this experiment to obtain transversely isotropic nanoporous structures with different porous geometry[55].

4.2.2. Microstructural characterization and mechanical testing

X-ray diffraction (XRD) and transmission electron microscopy (TEM) were employed to verify the amorphous state of the thin films. Rutherford backscattering spectroscopy (RBS) and Scanning electron microscopy (SEM) were used to determine composition of the amorphous thin film and observe the porous morphology separately. The evolution of the synthesized Voronoi polyhedra on the free surface was investigated by performing interrupted dealloying experiments and monitoring the same sample region through SEM.

Unlike traditional engineering metals, NP metal foams are brittle [8, 30, 61]. Hence traditional mechanical testing methods such as microtensile or microbending experiments turns out to be difficult [62]. Instead, experimental testing of mechanical properties of NP materials are usually carried out by Nanoindentation Tests [61, 63-65] and Micropillar Compression Tests [62, 66]. In this work, nanoindentation tests were

performed on TriboIndenter test system (Hysitron Inc.) using calibrated diamond Berkovich indenter tip. Trapezoid loading function is applied with maximum load 5000 μN , loading /unloading times 20s and constant-load holding time 10s.

4.3 Results and discussion

Transversely isotropic NP Pt is synthesized by electrochemical dealloying amorphous single phased $\text{Pt}_x\text{Si}_{1-x}$ thin films. After dealloying, silicon is completely removed from the alloy as verified from RBS and TEM measurements [41]. Distinctly different to the commonly seen isotropic open cell structure of NP Pt [12] and NP Au [2, 52, 61, 62], this particular transversely isotropic structure has a hierarchical morphology: a concave hyperstructures resembling Voronoi tessellation on the free surface (transverse plane) and lying underneath, elongated ligaments and pores extends through the thickness. The as-dealloyed material is nanocrystalline Pt with a grain size around 5 nm as verified from Cross-sectional TEM. The measured ligament size (l , shown in Fig.4.1.) is 55~60 nm in elongated direction and 10 nm in diameter along the radial direction size (w , shown in Fig.4.1.). The development of this morphology results from a combination of factor of cosputtering parameters, initial alloy composition and thin film thickness as summarized by Antoniou et al [41]. Figure 4.1 presents a schematic of a typical cross-section of transverse isotropic NP Pt foam synthesized in this work. The schematic identifies two possible strut patterns: (a) elongated radially aligned struts/pores within each Voronoi hyperstructure near the free surface and (b) elongated struts/pores through thickness direction. The strut patterns are a result of the changes in the dealloying front propagation as outlined in Chapter 2. As described in Chapter 2, the size of the Voronoi polyhedra, and therefore the overall size of the radially aligned strut pattern is dictated by the externally applied voltage. Figure 4.2 shows SEM cross-sectional images of different dimensions of the radially aligned and elongated segments of the through thickness morphology of the Voronoi NP Pt foam. The first, Figs.4.2 (a) and (b), show the

morphology within a large Voronoi polyhedron, where the thickness of the radially aligned struts is spanning the entire thickness of the thin film. At large dealloying voltages when the Voronoi polyhedra are suppressed, only elongated struts through the thickness direction form as shown in Figs.4.2 (f) and (g). Figs. 4.2 (c), (d) and (e) show the morphology of NP struts in between the above extremes. We emphasize that this morphology is observed for samples in sets A and B.

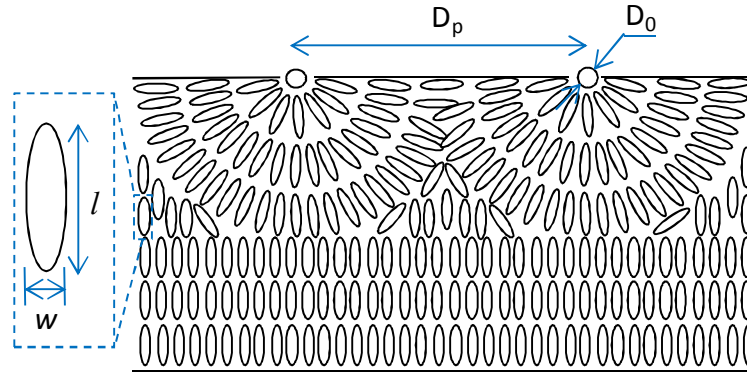


Figure 4.1 Schematic drawing of a typical cross-section of transverse isotropic NP Pt foam synthesized in this work.

Fig. 4.3(a) presents hardness values as a function of indentation depth for dealloyed samples from Sample Set B. The different symbols mark samples with different size of the Voronoi polyhedra and hence different dimensions of the overall radial zone. In order to limit substrate effects, the maximum indentation depth was chosen to be <20% of thin film thickness. The results show hardness enhancement of samples with large radial zone: hardness values increase to nearly three times comparing to the samples with isotropic open cell structure and nearly two times comparing to elongated vertically aligned structure. Fig. 4.3 (b) shows hardness as a function of indentation depth is normalized with the average ligament size (~60 nm) for different polyhedron dimensions. It is observed that the measured hardness reaches a steady state when the indentation depth reaches one cell size. This result is consistent with observations of indentation in bulk metal foams.

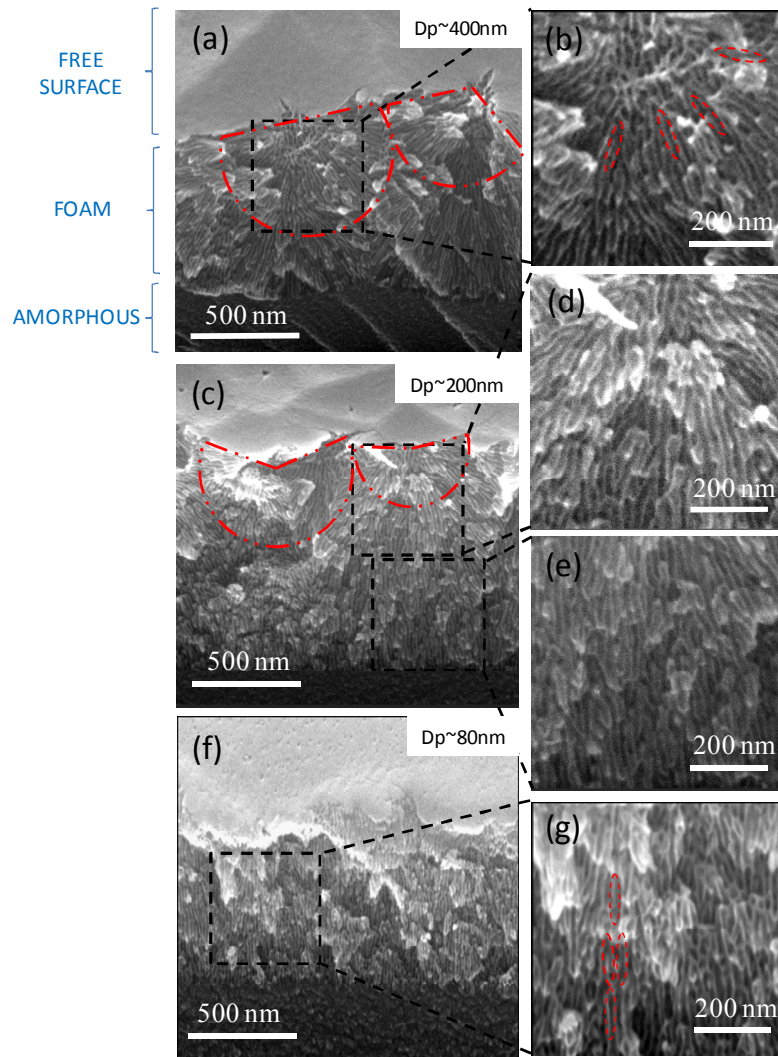


Figure 4.2 SEM cross-sectional images with (a) big Voronoi polyhedron size where radial emanation of ligaments and pores well preserved and its enlarged view (b); (f) small Voronoi polyhedron size where ligaments and pores align vertically through the thickness and its enlarged view (g); (c) polyhedron size in between shows a transformational morphology and its enlarged views (d) and (e). For clearer demonstration, spherical parts of dealloying fronts and several ligaments and pores are highlighted in red dotted line

Symbol	Polygon Size (nm)	Ligament		Dp
		Size (nm)	STDEV (nm)	
■	149.3	59.8	7.3	>130nm
◆	151.8	57.4	8.4	
●	112.9	56.7	8.1	In Between
■	61.8	59.0	6.6	<80nm
●	73.3	58.7	7.1	
□	N/A	N/A	N/A	Isotropic

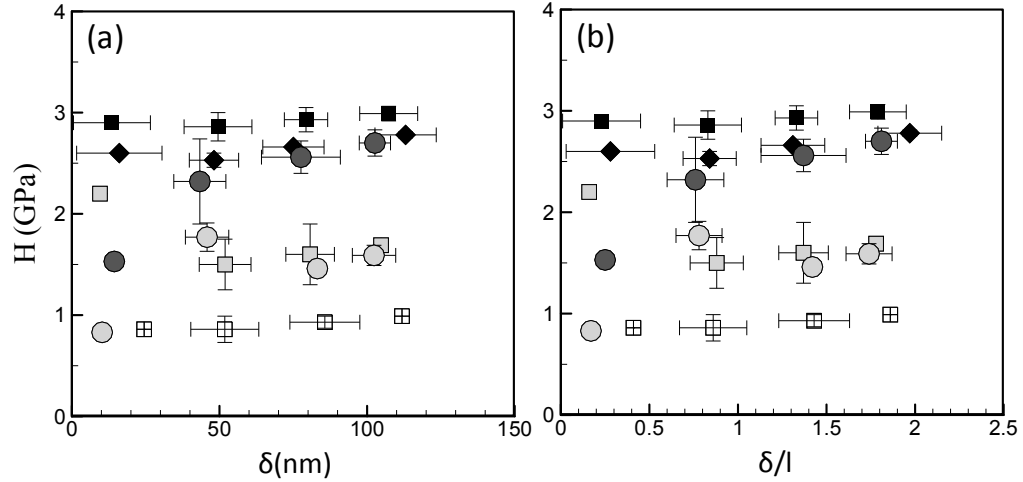


Figure 4.3 Hardness values (including standard deviation) as a function of (a) indentation depth δ and (b) indentation depth δ normalized by ligament size l for as-dealloyed samples in sample set B (detailed in Table 2.1) and isotropic open cell sample. Polygon sizes (D_p) and ligament length (l) are indicated in the legend.

The reduced modulus, E_r as a function of indentation depth is shown on Fig. 4.4

(a). The reduced modulus relates to the modulus of the sample through:

$$\frac{1}{E_r} = \frac{(1-\nu_i^2)}{E_i} + \frac{(1-\nu_s^2)}{E_s} \quad (1)$$

where the subscript i indicates a property of the indenter material and subscript s represents a property of sample, in our case, is the foam. For a diamond indenter tip, E_i is 1140 GPa and Poisson's ratio ν_i is 0.07. The poisson's ratio for the sample is assumed to be ν_s 0.2. The calculated Young's modulus E_s from E_r is presented in Fig 4.4 (b) and (c). Note that using the parameters given above, the value from E_s and E_r are almost identical, which goes in consistent with literature [94]. The Young's modulus also shows a similar

trend as hardness/yield strength: comparing to isotropic structure and elongated vertically aligned structure, E of samples with large radial zone increase to around two times and 1.3 times separately. It is worthy to point out here that this both strength and stiffness enhancement mechanism is distinctly different from the “size effect”, in which case even though the yield stress of NP metals increases strongly with decreasing ligament size has been widely reported [31, 62, 63, 75], negligible effect of sample size on Young’s modulus has been shown [34, 67].

As what we briefly mentioned in the introduction, the reason of the property enhancement could be due to (I) the difference in as-dealloyed sample composition; (II) the difference in relative density as the proposed by Gibson-Ashby scaling law; (III) Size effect introduced by ligaments/polycrystalline grain size. TEM has shown the NP Pt samples in this work are uniformly nanocrystalline with grain size of 5 nm. RBS and TEM observations confirm the complete elimination of the amorphous platinum silicide phase and the removal of Si [41]. So the difference of strength caused by composition is negligible in this case. The resulting NP structure ligament/pore size in this study is presented in Fig. 4.3 (the legend), the average ligament/pore sizes and size distribution (standard deviation) as well as nanocrystalline with grain sizes are comparable so that difference in their relative densities and size effect should be viewed insignificant.

The difference in strength and modulus are hence believed to be due to the geometrical arrangement of struts. We present here our *preliminary analysis* using analytical descriptions of i) plastic hinge formation and ii) failure of struts by elastic buckling for the radially aligned, the anisotropic (elongated) struts and for the isotropic struts. We emphasize that for bulk *metal* foams, the E/σ ratio is such that elastic bending is not possible for most geometries and failure in the struts occurs due to plastic hinge formation. In this system, we do not know the precise values of strut modulus and strength so we will consider both mechanisms.

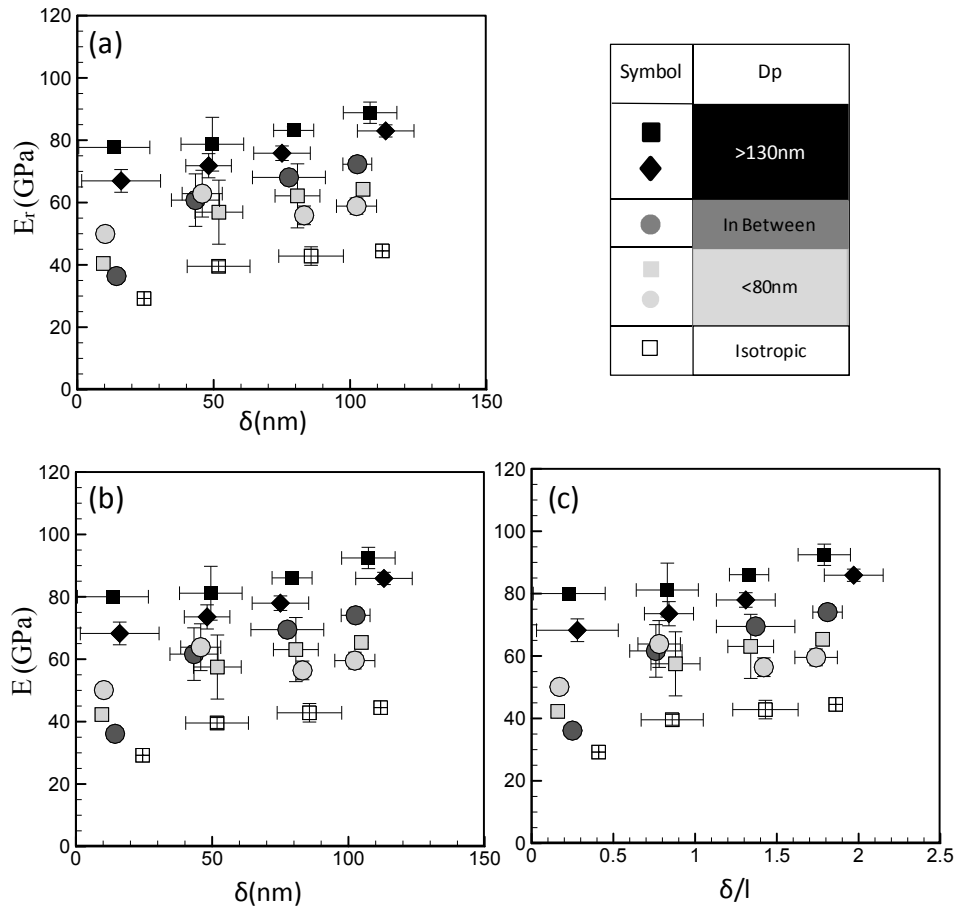


Figure 4.4 (a) Reduced modulus (including standard deviation) as a function of indentation depth δ . Calculated Young's modulus as a function of (b) indentation depth δ and (c) indentation depth δ normalized by ligament size l for as-dealloyed samples in sample set B (detailed in Table 2.1) and isotropic open cell sample.

We first explore the difference in strength due to different geometrical arrangements of struts.

(i) Failure by plastic collapse

Complicated as the NP network geometry is, general in plane loading of idealized foam structure is considered the first step towards understanding the more complex behavior of real 3D NP foam structure. As we already mentioned, three types of representative cell structures (ligament network geometry) are drawing attention, the

radial distributed ligament structure (radial cell for short), elongated ligament structure (elong. cell for short) and common seen isotropic open cell structure (iso. cell for short).

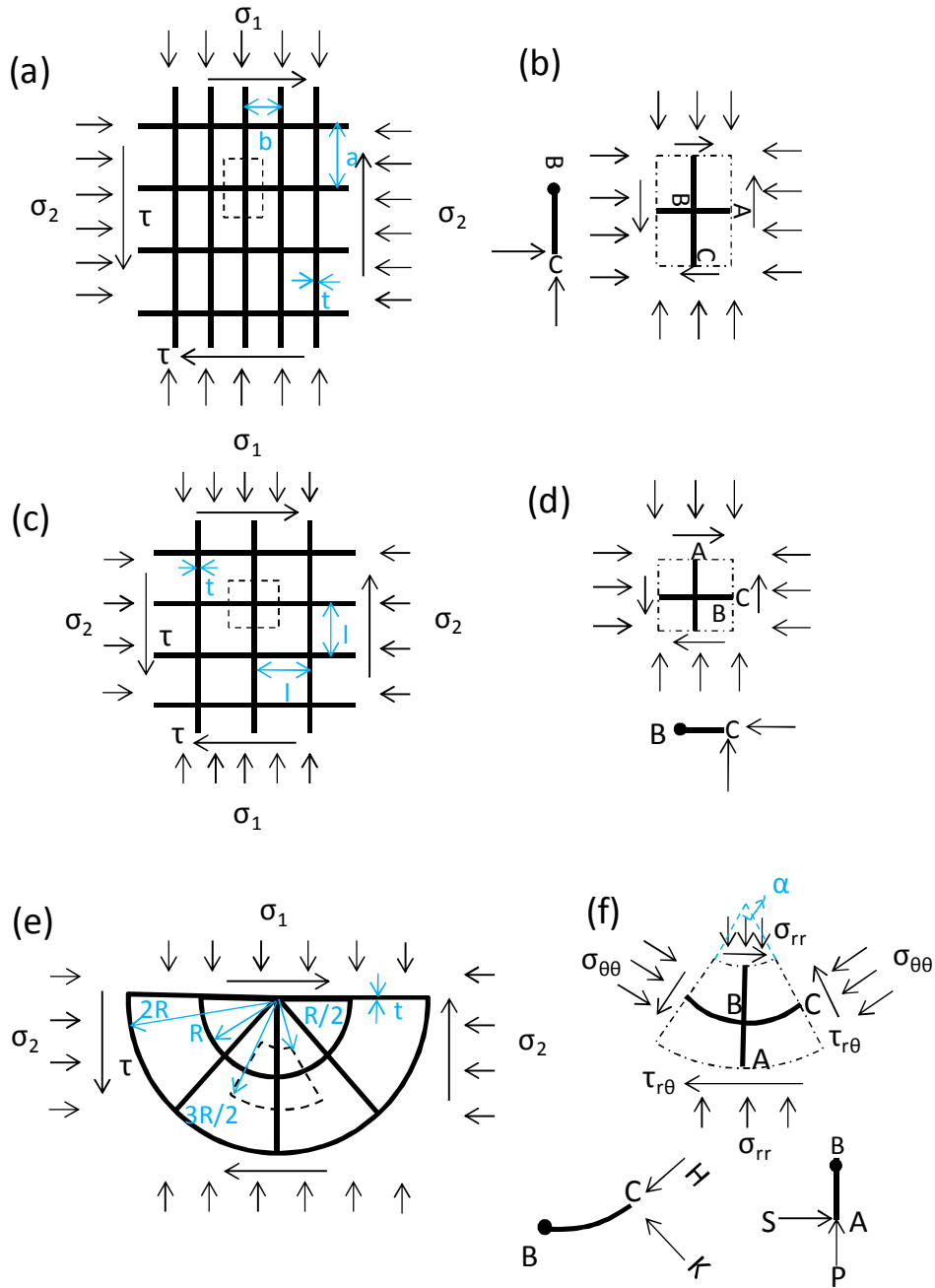


Figure 4.5 Under a general in plane stress state, (a) rectangular (elongated) cell periodic structure and (b) a unit cell; (c) square (isotropic) cell and (d) a unit cell; (e) half circle (radially distributed ligament) cell and a representative local part (f)

Geometrically, elongated ligament structure could be viewed as rectangular cell (as shown in Fig. 4.5(a)). Wang and McDowell [79] derived effective compressive strength for rectangular cell structure detailed as below. Consider the cell wall behavior to be elastic-perfectly plastic for a bending dominated beam, the fully plastic moment for a perfectly straight plastic beam under combined bending moment and extensional stress is modified by the shift of the neutral axis due to axial stress[95].

$$M_{p_straight} = \frac{1}{4} \sigma_{ys} c t^2 \left(1 - \left(\frac{\sigma}{\sigma_{ys}} \right)^2 \right) \quad (4.1)$$

The fully plastic limit moment is chosen here to represent the complete loss of its capacity to carry further load. A single unit cell of the periodic rectangular cell structure is shown in Fig. 4.5 (b), where a and b ($a > b$) are unit cell length and width, t and c are in plane and out of plane (into paper) cell wall thickness. By equating maximum bending moment to M_p , Wang and McDowell [79] gave the initial yield surface as shown in Eq.(4.2):

$$\sigma_{pl}^{elong} = \max \left\{ \left[\frac{a}{b} \left(\frac{\sigma_2}{\sigma_{ys}} \right)^2 + 2 \frac{|\tau|}{\sigma_{ys}} - \frac{(t)^2}{ab} \right], \left[\frac{b}{a} \left(\frac{\sigma_1}{\sigma_{ys}} \right)^2 + 2 \frac{|\tau|}{\sigma_{ys}} - \frac{(t)^2}{ab} \right] \right\} = 0 \quad (4.2)$$

In the indentation test, the most-easy-to-fail unit cell is under the indenter head. In this special location, no shear stress appears on the cell due to symmetry, also σ_1 is much larger than σ_2 . Hence Eq. (4.2) reduces to:

$$\sigma_{pl}^{elong} = \frac{t}{b} \sigma_{ys} \quad (4.3)$$

Note that isotropic open cell (see Fig. 4.5 (c) and (d)) is geometrically square cell structure which is just one special case of rectangular structure with both unit cell length and width to be l . Hence the effective initial yield surface reduces to:

$$\sigma_{pl}^{iso} = \max \left\{ \left[\left(\frac{\sigma_2}{\sigma_{ys}} \right)^2 + 2 \frac{|\tau|}{\sigma_{ys}} - \frac{t^2}{l^2} \right], \left[\left(\frac{\sigma_1}{\sigma_{ys}} \right)^2 + 2 \frac{|\tau|}{\sigma_{ys}} - \frac{t^2}{l^2} \right] \right\} = 0 \quad (4.4)$$

In the case of indentation, for the same reason as rectangular cell, Eq. (4.4) reduces to:

$$\sigma_{pl}^{elong} = \frac{t}{l} \sigma_{ys} \quad (4.5)$$

For the benefit of comparing the strength between different cell struts in a reasonable condition, relative density of the struts should set to be the same. The relative densities of various cell struts are shown in table 4.1. By defining $a/b=m$ ($m>1$) as the aspect ratio of a single cell unit, setting relative densities to be the same yields:

$$b = \frac{m+1}{3m} l \quad (4.6)$$

Substitute Eq. (4.6) into Eq. (4.3) yields:

$$\sigma_{pl}^{elong} = \frac{t}{b} \sigma_{ys} = \frac{t}{\frac{m+1}{3m} l} \sigma_{ys} > \sigma_{pl}^{iso} \quad (4.7)$$

This analytical results show that under same relative density, elongated cell strut tends to be stronger comparing to corresponding isotropic open cell, which gives an explanation of the observed experimental results.

For a radially distributed ligament structure, there is no global unit cell due to lack of periodic structure. But there exist periodic units within the half circle with same radius, one of the “unit cells” shown in Fig 4.5 (e) in dotted line. This unit cell is the most-easy-to-fail cell under the indenter head. Hence, we’ll analyze this structure based on this particular cell. The fully plastic moment for a perfectly curved plastic beam under combined bending moment and extensional stress is:

$$M_{p_curve} = \sigma_{ys} c \left(\frac{t^2}{4} + e^2 \right) \left(1 - \left(\frac{\sigma}{\sigma_{ys}} \right)^2 \right) \quad (4.8)$$

where e is the distance from the center of gravity axis to the neutral axis due to the shape of curved beam. Similar to the derivation in rectangular structure, the forces within the strut AB are:

$$P = \sigma_{rr} \frac{3R\alpha}{2} c, \quad S = \tau_{r\theta} \frac{R\alpha}{2} c \quad (4.9)$$

The axial stress and the bending moment within AB (straight beam) are given by

$$\sigma_a = \frac{P}{tc} = \sigma_{rr} \frac{3R\alpha}{2t}, \quad |M_{max}| = S \frac{R}{2} = \tau_{r\theta} \frac{R^2\alpha}{4} c \quad (4.10)$$

Setting $M_{max}=M_{P_straight}$, the yield function is given by

$$\left(\frac{\sigma_{rr}}{\sigma_{ys}}\right)^2 + \frac{4}{9R\alpha} \frac{|\tau_{r\theta}|}{\sigma_{ys}} = \frac{4t^2}{(3R\alpha)^2} \quad (4.11)$$

On the other hand, forces within the strut BC are:

$$H = \sigma_{\theta\theta}Rc, \quad K = \tau_{r\theta}Rc \quad (4.12)$$

The axial stress and the bending moment within BC (curved beam) are given by

$$\sigma_a = \frac{H}{tc} = \sigma_{\theta\theta} \frac{R}{t}, \quad |M_{max}| = K \frac{\alpha R}{2} = \tau_{r\theta} \frac{R^2 \alpha}{2} c \quad (4.13)$$

Setting $M_{max}=M_{P_curved}$, the yield function is given by

$$\left(\frac{\sigma_{\theta\theta}}{\sigma_{ys}}\right)^2 + \frac{2\alpha t^2}{t^2+4e^2} \frac{|\tau_{r\theta}|}{\sigma_{ys}} = \frac{t^2}{R^2} \quad (4.14)$$

Combining Eqs. (4.11) and (4.14) gives the initial yield surface of radial cell as:

$$\sigma_{pl}^{radial} = \max \left\{ \left[\left(\frac{\sigma_{rr}}{\sigma_{ys}}\right)^2 + \frac{4}{9R\alpha} \frac{|\tau_{r\theta}|}{\sigma_{ys}} - \frac{4t^2}{(3R\alpha)^2} \right], \left[\left(\frac{\sigma_{\theta\theta}}{\sigma_{ys}}\right)^2 + \frac{2\alpha t^2}{t^2+4e^2} \frac{|\tau_{r\theta}|}{\sigma_{ys}} - \frac{t^2}{R^2} \right] \right\} = 0 \quad (4.15)$$

In the indentation test, the special location we analyzed here, no shear stress appears on the cell due to symmetry; also σ_{rr} is significantly larger than $\sigma_{\theta\theta}$, so the effective compressive strength for radial structure can be obtained by reducing Eq. (4.15) to

$$\sigma_{pl}^{radial} = \frac{t}{3R\alpha/2} \sigma_{ys} \quad (4.16)$$

By setting relative density of radial cell and isotropic cell to be the same, we get


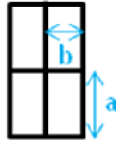

$$R = \left(\frac{1}{\alpha} + 1\right) l \quad (4.17)$$

Plugging in the Eq. (4.17) into (4.16),

$$\sigma_{pl}^{radial} = \frac{t}{\left(\frac{3}{2} + \frac{3\alpha}{2}\right)l} \sigma_{ys} < \sigma_{pl}^{iso} \quad (4.18)$$

These analytical results show that under same relative density, radial cell strut tends to be weaker comparing to corresponding isotropic open cell, which goes contradictory to the observed experimental results.

Table 4.1 The relative densities of various cell struts

Structure name	Isotropic cell	Elongated cell	Radial cell
Schematic			
Relative Density $\rho = \rho_{\text{foam}} / \rho_{\text{solid}}$	$3t/l$	$3(a+b)t/ab$	$3(1+\alpha)t/\alpha R$

(ii) Failure by elastic buckling

Another possible failure mode is elastic buckling. Euler equation for columns with no consideration for lateral forces is given in Eq. (4.19)

$$F_c = \frac{\pi^2 EI}{(KL)^2} \quad (4.19)$$

Where F is critical force (vertical load on column), E is Young's modulus, I is area moment of inertia of the cross section, and L is the unsupported length of column.

For isotropic cell ligament, the critical force is

$$F_c^{iso} = \frac{\pi^2 EI}{(KL)^2} \quad (4.20)$$

where l is ligament length. The ligament cross sections keep the same for isotropic cell, elongated cell and radially distributed cell. Hence we assume area moment of inertia is constant here. K is also constant as we assume the two ends of the ligaments be fixed for all three types of ligaments.

Comparatively, the critical forces of elongated cell ligament and radially distributed cell ligament with same relative density are shown in Eqs. (4.21) and (4.22) separately.

$$F_c^{elong} = \frac{\pi^2 EI}{(Ka)^2} = \left(\frac{2}{m+1}\right)^2 F_c^{iso} < F_c^{iso} \quad (m > 1) \quad (4.21)$$

$$F_c^{rad} = \frac{1}{\cos \theta} F_c^{elong} > F_c^{elong} \quad (4.22)$$

The results show that radially distributed cell ligament do have higher strength comparing to elongated one, which is consistent with experimental results, while elongated cell ligament has a lower calculated strength comparing to isotropic cell ligament, which is contradictory to the conclusion of experiments.

As we have already shown above, none of the two failure mode can explain everything by its own. The inconsistency of a single failure mode to the experimental observations indicates that even though in microscale and/or on individual ligament, one of the two modes may dominate, the overall strut may be governed by a combination of the two modes.

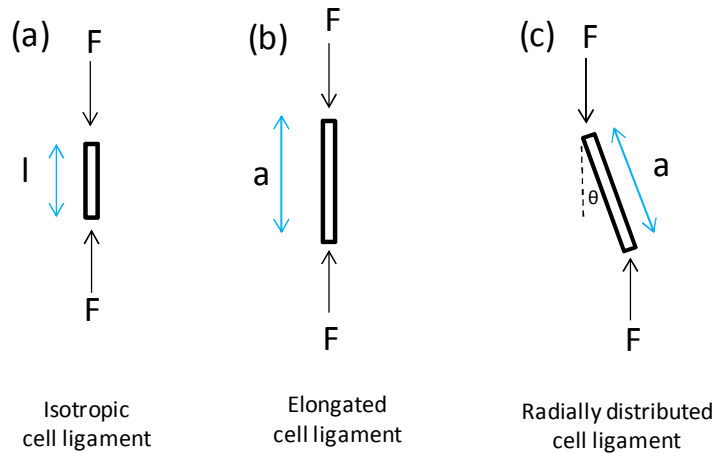


Figure 4.6 Ligaments under compression with no consideration of lateral forces for (a) isotropic cell ligament; (b) elongated cell ligament and (c) radially distributed cell ligament

Next we explore the difference in stiffness due to different geometrical arrangements of struts.

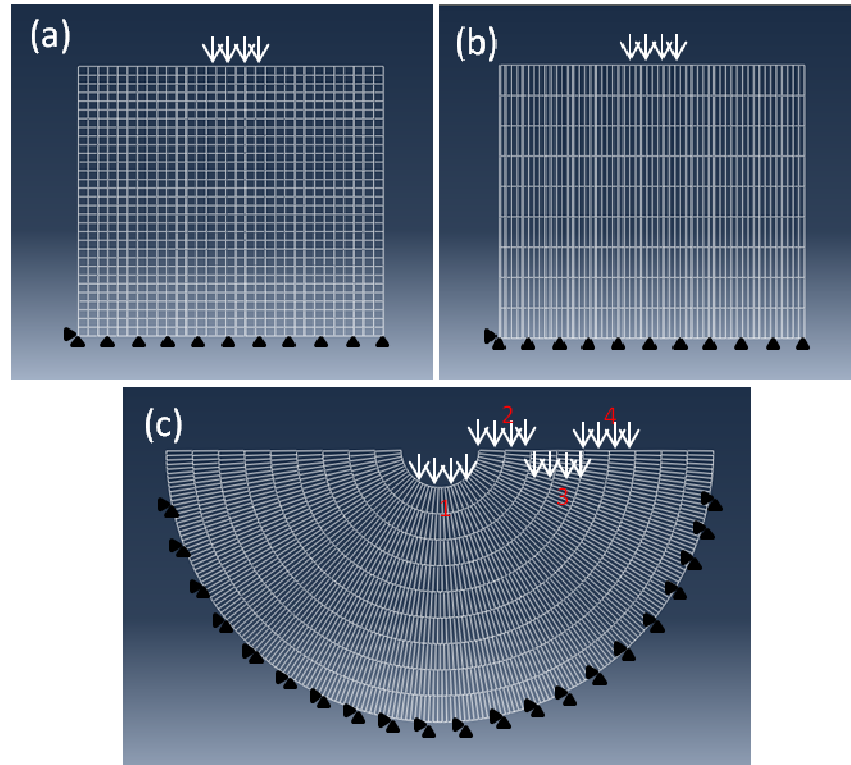


Figure 4.7 ABAQUS modeling of (a) isotropic cell structure, (b) elongated cell structure and (c) radial cell structure with center loading (position 1) and eccentric loading at different locations (position 2,3,4, with small, medium, and large amount of shift of loading center from the structure center point, separately). All the three structure have same relative density.

ABAQUS is used to carry out finite element modeling. 2D Model structures and loading locations of three above mentioned structures are shown in Fig. 4.7. For radial cell structure, one center loading and three eccentric loading with increasing level of shifting from center are conducted. To avoid boundary effect, loading is restricted far from the boundary. The relative density of the three types of cell structure is kept constant. Several other parameters are also set the same including thickness of cell structure and areas on which the reaction forces are extracted. The stiffness comparison

for different cell geometries of several loading conditions is shown in Fig. 4.8. The stiffness of other geometries and loading conditions are scaled by isotropic cell structure for better illustration. Stiffness of center loading on radial cell structure is the highest, while the eccentric loading is the smallest and the amount of shift of loading locations from the structure center point seems to have trivial effects on calculated stiffness. In the real case, the stiffness of distributed cell structure should be an averaging of the center loading and eccentric loading. Having said that, one can still see the stiffness for radial cell structure with center loading is around 1.3 times of the stiffness of elongated cell structure and around 2 times of the stiffness of isotropic cell structure, which is consistent with the trend of the experimental data we obtained in this study.

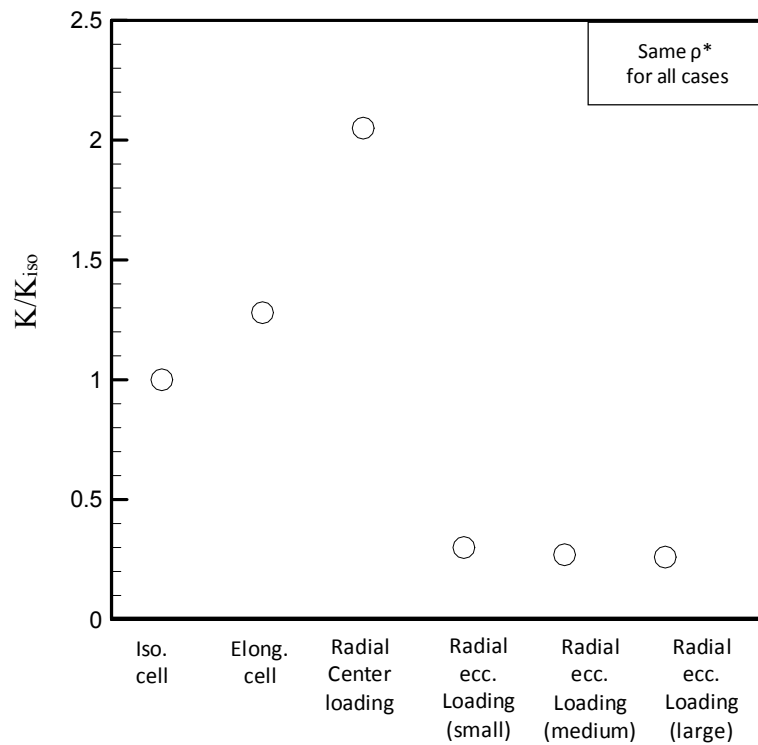


Figure 4.8 Stiffness comparison for different cell geometries of several loading conditions. Small, medium and large in parenthesis after eccentric loading means the amount of shift of loading center from the structure center point. Relative densities are identical for all cases.

It should be mentioned that additional work needs to be done by establishing a more precise FEA model of higher similarity with the resulting foam morphology and indentation process. A higher consistency of the simulation results with the experimental observation is expected based on the future model.

4.4 Summary

In summary, we synthesized transversely isotropic NP Pt metal foam by dealloying amorphous $\text{Pt}_x\text{Si}_{1-x}$ thin films. The relative densities and ligament sizes of resulting foam are similar while 3-D network geometry of ligaments and pores transforms from radial emanation to vertical alignment as the polygon size decreases. The network with radial emanated distribution of ligaments has stiffness and hardness discernibly higher than the network with vertically aligned structure/isotropic open cell structure. This morphological variation could be finely controlled by the dealloying potential as we described in the previous work (previous chapters). This study is important in providing a possible new way of refining mechanical property of NP metal foams.

CHAPTER 5

SUMMARY AND FUTURE WORK

This work has focused on three aspects: synthesis of a novel nanoporous platinum foam structure with transverse isotropy, investigation of the origin of this type of structure by proposing a preferential initiation mechanism of the dealloying process, and the study of mechanical behavior of NP Pt under the effect of ligament network geometry. Combining these aspects has yielded a better understanding of the underlying mechanisms behind the formation of the new type of NP Pt structure that can allow for further exploration of its applications.

We demonstrate that, in addition to the commonly seen isotropic open cell, NP Pt foam with transverse isotropy could be synthesized from amorphous PtSi alloy by dealloying. We examine the hierarchical foam structure and further report the degree of control one can have during synthesis of NP Pt foam assembled during dealloying. The externally applied potential controls the size of the Voronoi polyhedra on the free surface (first level of anisotropy) as well as the underlying ligaments/pores distribution (second level of anisotropy). We rationalize this phenomenon by demonstrating the significant effect of surface roughness and externally applied dealloying potential on the preferential initiation issue during electrochemical dealloying process. Finally, we explore the mechanical behavior of the synthesized NP Pt and demonstrate that foam network geometry could have some influence the tested mechanical property.

The study can be important in finely tuning well-defined NP foam morphology to improve their functionality and biocompatibility by varying external experimental parameters such as surface nanoarchitecture manipulation.

Future work includes:

- 1) Improve finite element modeling to address the foam network geometrical effect on mechanical property. Instead of modeling the porous structure as a

frame, a constitutive model that captures the heterogeneous deformation is needed. For example, in micropolar theory the stress state at a material point depends on the strains and their gradients in the neighboring region. The micropolar constitutive model would allow for additional degrees of freedom to be used to define any heterogeneous deformation that exists at the strut level. For NP metal foams, the unit cell is a representative group of ligaments and pores;

- 2) Introducing nanoarchitecture on the free surface using masks to further validate preferential initiation mechanism and gain higher-level control of the synthesized foam morphology.
- 3) Examine the implications of the initiation mechanism at preferential sites to understand how chemical and mechanical parameters are coupled to cause the surface instability that enables the self assembly of transversely isotropic NP metal structures.

REFERENCES

- [1] R. Zeis, *et al.*, "Platinum-plated nanoporous gold: An efficient, low Pt loading electrocatalyst for PEM fuel cells," *Journal of Power Sources*, vol. 165, pp. 65-72, 2007.
- [2] Y. Ding, *et al.*, "Nanoporous gold leaf: "Ancient technology"/advanced material," *Advanced Materials*, vol. 16, pp. 1897-1900, Nov 4 2004.
- [3] J. S. Yu, *et al.*, "Formation of Rosette-Like Nanopatterns by Selective Corrosion of Metallic Glass," *Japanese Journal of Applied Physics*, vol. 47, pp. 8678-8680, Nov 2008.
- [4] A. D. Gautam Gupta, Antonia Antoniou and Amit Misra "Trasmembrane proteins on Nanoporous metals," *in preparation*.
- [5] D. Yi, *et al.*, "Nanoporous gold leaf: "Ancient technology"/advanced material," *Advanced Materials*, vol. 16, p. 4, November 4 2004.
- [6] S. Parida, *et al.*, "Volume change during the formation of nanoporous gold by dealloying," *Physical Review Letters*, vol. 97, p. 035504, Jul 21 2006.
- [7] X. Lu, *et al.*, "Dealloying of Au-Ag thin films with a composition gradient: Influence on morphology of nanoporous Au," *Thin Solid Films*, vol. 515, pp. 7122-7126, 2007.
- [8] R. Li and K. Sieradzki, "Ductile-Brittle Transition in Random Porous Au," *Physical Review Letters*, vol. 68, pp. 1168-1171, Feb 24 1992.
- [9] F. Kertis, *et al.*, "Structure/Processing Relationships in the Fabrication of Nanoporous Gold," *Jom*, vol. 62, pp. 50-56, Jun 2010.
- [10] A. J. Forty, "Corrosion Micro-Morphology of Noble-Metal Alloys and Depletion Gilding," *Nature*, vol. 282, pp. 597-598, 1979.
- [11] D. V. Pugh, *et al.*, "Formation of nanoporous platinum by selective dissolution of Cu from Cu_{0.75}Pt_{0.25}," *Journal of Materials Research*, vol. 18, pp. 216-221, Jan 2003.
- [12] J. C. Thorp, *et al.*, "Formation of nanoporous noble metal thin films by electrochemical dealloying of Pt_xSi_{1-x}," *Applied Physics Letters*, vol. 88, pp. 033110 -3 Jan 16 2006.
- [13] H. Q. Li and A. Misra, "A dramatic increase in the strength of a nanoporous Pt-Ni alloy induced by annealing," *Scripta Materialia*, vol. 63, pp. 1169-1172, Dec 2010.
- [14] H. Q. Li, *et al.*, "Synthesis and characterization of nanoporous Pt-Ni alloys," *Applied Physics Letters*, vol. 95, p. 201902 Nov 16 2009.
- [15] J. R. Hayes, *et al.*, "Monolithic nanoporous copper by dealloying Mn-Cu," *Journal of Materials Research*, vol. 21, pp. 2611-2616, Oct 2006.
- [16] U. S. Min and J. C. M. Li, "The Microstructure and Dealloying Kinetics of a Cu-Mn Alloy," *Journal of Materials Research*, vol. 9, pp. 2878-2883, Nov 1994.
- [17] Pickerin.Hw and C. Wagner, "Electrolytic Dissolution of Binary Alloys Containing a Noble Metal," *Journal of the Electrochemical Society*, vol. 114, pp. 698-&, 1967.

- [18] M. J. Pryor and J. C. Fister, "The Mechanism of Dealloying of Copper Solid-Solutions and Intermetallic Phases," *Journal of the Electrochemical Society*, vol. 131, pp. 1230-1235, 1984.
- [19] J. Rosler and D. Mukherji, "Design of nanoporous superalloy membranes for functional applications," *Advanced Engineering Materials*, vol. 5, pp. 916-18, 2003.
- [20] J. Rosler, *et al.*, "Fabrication of nanoporous Ni-based superalloy membranes," *Acta Materialia*, vol. 53, pp. 1397-1406, Mar 2005.
- [21] A. Dursun, *et al.*, "A steady-state method for determining the dealloying critical potential," *Electrochemical and Solid State Letters*, vol. 6, pp. B32-B34, Aug 2003.
- [22] A. Dursun, *et al.*, "Dealloying of Ag-Au alloys in halide-containing electrolytes - Affect on critical potential and pore size," *Journal of the Electrochemical Society*, vol. 150, pp. B355-B360, Jul 2003.
- [23] J. R. Calvert DC, "XLI.—Action of acids upon metals and alloys," *Journal of the Chemical Society*, vol. 19, pp. 434 - 454, 1866.
- [24] S. G. Corcoran, *et al.*, "In situ small angle neutron scattering investigation of Ag_{0.7}Au_{0.3} dealloying," *Materials Research Society Symposium Proceedings*, vol. 376, pp. 377-382, November 28 - December 1, 1994 1995.
- [25] K. Wagner, *et al.*, "Dealloying below the critical potential," *Journal of the Electrochemical Society*, vol. 144, pp. 3545-3555, Oct 1997.
- [26] J. Erlebacher and K. Sieradzki, "Pattern formation during dealloying," *Scripta Materialia*, vol. 49, pp. 991-996, Nov 2003.
- [27] Z. Qi, *et al.*, "Formation and Characterization of Monolithic Nanoporous Copper by Chemical Dealloying of Al-Cu Alloys," *The Journal of Physical Chemistry C*, vol. 113, pp. 6694-6698, 2009.
- [28] R. Morrish, *et al.*, "Formation of nanoporous Au by dealloying Au Cu thin films in HNO₃," *Scripta Materialia*, vol. 64, pp. 856-859, May 2011.
- [29] R. P. Tischer and H. Gerischer, "Elektrolytische Auflösung Von Gold-Silber-Legierungen Und Die Frage Der Resistenzgrenzen," *Zeitschrift Fur Elektrochemie*, vol. 62, pp. 50-60, 1958.
- [30] J. Biener, *et al.*, "Microscopic failure behavior of nanoporous gold," *Applied Physics Letters*, vol. 87, pp. -, Sep 19 2005.
- [31] J. Biener, *et al.*, "Size effects on the mechanical behavior of nanoporous Au," *Nano Letters*, vol. 6, pp. 2379-2382, Oct 11 2006.
- [32] A. J. Forty and P. Durkin, "A Micro-Morphological Study of the Dissolution of Silver-Gold Alloys in Nitric-Acid," *Philosophical Magazine a-Physics of Condensed Matter Structure Defects and Mechanical Properties*, vol. 42, pp. 295-318, 1980.
- [33] A. J. Forty and G. Rowlands, "A Possible Model for Corrosion Pitting and Tunnelling in Noble-Metal Alloys," *Philosophical Magazine a-Physics of Condensed Matter Structure Defects and Mechanical Properties*, vol. 43, pp. 171-188, 1981.
- [34] A. M. Hodge, *et al.*, "Ag effects on the elastic modulus values of nanoporous Au foams," *Journal of Materials Research*, vol. 24, pp. 1600-1606, Apr 2009.

- [35] Y. Sun and T. J. Balk, "A multi-step dealloying method to produce nanoporous gold with no volume change and minimal cracking," *Scripta Materialia*, vol. 58, pp. 727-730, May 2008.
- [36] K. Sieradzki, *et al.*, "The dealloying critical potential," *Journal of the Electrochemical Society*, vol. 149, pp. B370-B377, Aug 2002.
- [37] T. P. Moffat, *et al.*, "Electrochemical and Scanning Tunneling Microscopic Study of Dealloying of Cu₃Au," *Journal of the Electrochemical Society*, vol. 138, pp. 3224-3235, Nov 1991.
- [38] Pickerin.Hw, "Stress Corrosion Via Localized Anodic Dissolution in Cu-Au Alloys," *Corrosion*, vol. 25, pp. 289-&, 1969.
- [39] J. I. Gardiazabal and J. R. Galvele, "Selective Dissolution of Cd-Mg Alloys .1. Static Samples," *Journal of the Electrochemical Society*, vol. 127, pp. 255-258, 1980.
- [40] J. I. Gardiazabal and J. R. Galvele, "Selective Dissolution of Cd-Mg Alloys .2. Rotating-Ring Disk Electrode," *Journal of the Electrochemical Society*, vol. 127, pp. 259-265, 1980.
- [41] A. Antoniou, *et al.*, "Controlled nanoporous Pt morphologies by varying deposition parameters," *Applied Physics Letters*, vol. 95, pp. 073116-073118 2009.
- [42] L. Sun, *et al.*, "Fabrication of nanoporous nickel by electrochemical dealloying," *Chemistry of Materials*, vol. 16, pp. 3125-3129, 2004.
- [43] Y. Ding and J. Erlebacher, "Nanoporous metals with controlled multimodal pore size distribution," *Journal of the American Chemical Society*, vol. 125, pp. 7772-7773, Jul 2 2003.
- [44] A. Katagiri and M. Nakata, "Preparation of a high surface area nickel electrode by alloying and dealloying in a ZnCl₂-NaCl melt," *Journal of the Electrochemical Society*, vol. 150, pp. C585-C590, Sep 2003.
- [45] C. X. Ji and P. C. Searson, "Fabrication of nanoporous gold nanowires," *Applied Physics Letters*, vol. 81, pp. 4437-4439, Dec 2 2002.
- [46] Z. Liu and P. C. Searson, "Single nanoporous gold nanowire sensors," *Journal of Physical Chemistry B*, vol. 110, pp. 4318-4322, Mar 9 2006.
- [47] A. Dursun, *et al.*, "Probing the dealloying critical potential - Morphological characterization and steady-state current behavior," *Journal of the Electrochemical Society*, vol. 152, pp. B65-B72, 2005.
- [48] J. Erlebacher, "An atomistic description of dealloying - Porosity evolution, the critical potential, and rate-limiting behavior," *Journal of the Electrochemical Society*, vol. 151, pp. C614-C626, 2004.
- [49] H. W. Pickering, "Characteristic Features of Alloy Polarization Curves," *Corrosion Science*, vol. 23, pp. 1107-&, 1983.
- [50] K. Sieradzki, *et al.*, "Computer-Simulations of Corrosion - Selective Dissolution of Binary-Alloys," *Philosophical Magazine a-Physics of Condensed Matter Structure Defects and Mechanical Properties*, vol. 59, pp. 713-746, Apr 1989.
- [51] K. Sieradzki, "Curvature Effects in Alloy Dissolution," *Journal of the Electrochemical Society*, vol. 140, pp. 2868-2872, Oct 1993.
- [52] J. Erlebacher, *et al.*, "Evolution of nanoporosity in dealloying," *Nature*, vol. 410, pp. 450-453, Mar 22 2001.

- [53] J. Hai-Jun, *et al.*, "Nanoporous Au-Pt Alloys As Large Strain Electrochemical Actuators," *ACS Nano Letters*, vol. 10, pp. 187-94, 2010.
- [54] P. Wahl, *et al.*, "Adsorption-driven tuning of the electrical resistance of nanoporous gold," *Journal of Applied Physics*, vol. 108, p. 073706 (6 pp.), 2010.
- [55] A. A. Yuan Li, "Synthesis of transversely isotropic nanoporous platinum," *accepted, Scripta Materialia*.
- [56] J. Hai-Jun, *et al.*, "Sign-inverted surface stress-charge response in nanoporous gold," *Surface Science*, vol. 602, pp. 3588-94, 2008.
- [57] H.-J. Jin, *et al.*, "Nanoporous au-pt alloys as large strain electrochemical actuators," *Nano Letters*, vol. 10, pp. 187-194, 2010.
- [58] A. A. Y. Li, "Conditions for dealloying initiation in alloys near the parting limit," *in preparation*.
- [59] K. M. Liu Ran, and Antoniou Antonia, "Synthesis of polycrystalline nanoporous copper."
- [60] J. Biener, *et al.*, "Surface-chemistry-driven actuation in nanoporous gold," *Nature Materials*, vol. 8, pp. 47-51, 2009.
- [61] J. Biener, *et al.*, "Nanoporous Au: A high yield strength material," *Journal of Applied Physics*, vol. 97, pp. -, Jan 15 2005.
- [62] C. A. Volkert, *et al.*, "Approaching the theoretical strength in nanoporous Au," *Applied Physics Letters*, vol. 89, pp. -, Aug 7 2006.
- [63] M. Hakamada and M. Mabuchi, "Mechanical strength of nanoporous gold fabricated by dealloying," *Scripta Materialia*, vol. 56, pp. 1003-1006, Jun 2007.
- [64] D. Lee, *et al.*, "Microfabrication and mechanical properties of nanoporous gold at the nanoscale," *Scripta Materialia*, vol. 56, pp. 437-440, Mar 2007.
- [65] E. Seker, *et al.*, "The effects of post-fabrication annealing on the mechanical properties of freestanding nanoporous gold structures," *Acta Materialia*, vol. 55, pp. 4593-4602, Aug 2007.
- [66] M. D. Uchic, *et al.*, "Sample dimensions influence strength and crystal plasticity," *Science*, vol. 305, pp. 986-989, Aug 13 2004.
- [67] R. Brezny and D. J. Green, "The Effect of Cell-Size on the Mechanical-Behavior of Cellular Materials," *Acta Metallurgica Et Materialia*, vol. 38, pp. 2517-2526, Dec 1990.
- [68] J. R. Greer, *et al.*, "Size dependence of mechanical properties of gold at the micron scale in the absence of strain gradients," *Acta Materialia*, vol. 53, pp. 1821-1830, Apr 2005.
- [69] B. Wu, *et al.*, "Mechanical properties of ultrahigh-strength gold nanowires," *Nature Materials*, vol. 4, pp. 525-529, Jul 2005.
- [70] L. A. Zepeda-Ruiz, *et al.*, "Mechanical response of freestanding Au nanopillars under compression," *Applied Physics Letters*, vol. 91, pp. -, Sep 3 2007.
- [71] A. Mathur and J. Erlebacher, "Size dependence of effective Young's modulus of nanoporous gold," *Applied Physics Letters*, vol. 90, pp. -, Feb 5 2007.
- [72] L. J. Gibson and M. F. Ashby, *Cellular solids : structure and properties*, 2nd ed. Cambridge ; New York: Cambridge University Press, 1997.
- [73] T. Fujita, *et al.*, "Three-dimensional morphology of nanoporous gold," *Applied Physics Letters*, vol. 92, pp. -, Jun 23 2008.

- [74] H. J. Jin, *et al.*, "Deforming nanoporous metal: Role of lattice coherency," *Acta Materialia*, vol. 57, pp. 2665-2672, May 2009.
- [75] A. M. Hodge, *et al.*, "Scaling equation for yield strength of nanoporous open-cell foams," *Acta Materialia*, vol. 55, pp. 1343-1349, Feb 2007.
- [76] A. C. Fischer-Cripps, *Nanoindentation*, 2nd ed. New York: Springer, 2004.
- [77] A. A. Benzerga and N. F. Shaver, "Scale dependence of mechanical properties of single crystals under uniform deformation," *Scripta Materialia*, vol. 54, pp. 1937-1941, Jun 2006.
- [78] D. M. Dimiduk, *et al.*, "Size-affected single-slip behavior of pure nickel microcrystals," *Acta Materialia*, vol. 53, pp. 4065-4077, Sep 2005.
- [79] A. J. Wang and D. L. McDowell, "Yield surfaces of various periodic metal honeycombs at intermediate relative density," *International Journal of Plasticity*, vol. 21, pp. 285-320, 2005.
- [80] A. J. Wang and D. L. McDowell, "In-plane stiffness and yield strength of periodic metal honeycombs," *Journal of Engineering Materials and Technology-Transactions of the Asme*, vol. 126, pp. 137-156, Apr 2004.
- [81] T. G. Nieh, *et al.*, "Effect of cell morphology on the compressive properties of open-cell aluminum foams," *Materials Science and Engineering a-Structural Materials Properties Microstructure and Processing*, vol. 283, pp. 105-110, May 15 2000.
- [82] B. Jiang, *et al.*, "Processing of open cell aluminum foams with tailored porous morphology," *Scripta Materialia*, vol. 53, pp. 781-785, Sep 2005.
- [83] L. Moroni, *et al.*, "3D fiber-deposited scaffolds for tissue engineering: Influence of pores geometry and architecture on dynamic mechanical properties," *Biomaterials*, vol. 27, pp. 974-985, Oct 2006.
- [84] D. M. Liu, "Control of pore geometry on influencing the mechanical property of porous hydroxyapatite bioceramic," *Journal of Materials Science Letters*, vol. 15, pp. 419-421, Mar 1 1996.
- [85] M. D. Demetriou, *et al.*, "Amorphous metals for hard-tissue prosthesis," *JOM*, vol. 62, pp. 83-91, 2010.
- [86] J. C. Thorp, *et al.*, "Formation of nanoporous noble metal thin films by electrochemical dealloying of Pt_xSi_{1-x}," *Applied Physics Letters*, vol. 88, pp. 1-3, 2006.
- [87] M. D. Abramoff, *et al.*, "Image processing with imageJ," *Biophotonics International*, vol. 11, pp. 36-41, 2004.
- [88] M. S. Wu, *et al.*, "Electrodeposition of nanoporous nickel oxide film for electrochemical capacitors," *International Journal of Hydrogen Energy*, vol. 32, pp. 4153-4159, Dec 2007.
- [89] D. D. Zhao, *et al.*, "Preparation of hexagonal nanoporous nickel hydroxide film and its application for electrochemical capacitor," *Electrochemistry Communications*, vol. 9, pp. 869-874, May 2007.
- [90] M. S. Wu, *et al.*, "Morphological and structural studies of nanoporous nickel oxide films fabricated by anodic electrochemical deposition techniques," *Electrochimica Acta*, vol. 54, pp. 155-161, Dec 30 2008.

- [91] Y. Zhang, *et al.*, "Progress of electrochemical capacitor electrode materials: A review," *International Journal of Hydrogen Energy*, vol. 34, pp. 4889-4899, Jun 2009.
- [92] P. Simon and Y. Gogotsi, "Materials for electrochemical capacitors," *Nature Materials*, vol. 7, pp. 845-854, Nov 2008.
- [93] Y. Ding, *et al.*, "Metallic mesoporous nanocomposites for electrocatalysis," *Journal of the American Chemical Society*, vol. 126, pp. 6876-6877, Jun 9 2004.
- [94] W. C. Oliver and G. M. Pharr, "An Improved Technique for Determining Hardness and Elastic-Modulus Using Load and Displacement Sensing Indentation Experiments," *Journal of Materials Research*, vol. 7, pp. 1564-1583, Jun 1992.
- [95] P. G. Hodge, *Plastic analysis of structures*. New York,: McGraw-Hill, 1959.